## Chemical Evolution and Kilonova Implications of Post-Merger Accretion Disk Winds

Agnieszka Janiuk<sup>1,\*</sup>, Joseph Saji<sup>1</sup>, and Gerardo Urrutia<sup>1</sup>

Center for Theoretical Physics, Polish Academy of Sciences, Al. Lotnikow 32/46, 02-668 Warsaw, Poland

November 10, 2025

#### **ABSTRACT**

Context. Several gamma ray bursts have recently been associated with a kilonova emission. We study the mechanisms which could account for this effect, by means of radioactive decay of elements synthesized in accretion disk wind.

*Aims.* We model the r-process nucleosynthesis in the accretion disk wind system, associated with the prompt GRB phase. We compute the time-dependent GR MHD evolution of a GRB central engine where the newly formed black hole is accreting the mass from post-merger remnant. We explore the wind properties, for a range of the initial parameters of the system, and study representative cases for compact binary merger progenitors.

Methods. We compute a suite of 2D and 3D time-dependent General Relativistic numerical simulations with a tabulated 3-parameter equation of state that allows for evolution of chemical composition evolution of the accretion flow. The neutrino emission is accounted for by incorporating the leakage scheme, where neutrino optical depth is calculated along the radial rays. We parameterize the optically thick and thin tori with different values of the pressure maximum and entropy in the disk, while the strength of large-scale poloidal magnetic fields is parameterized according to the chosen gas-to-magnetic pressure ratio. To probe the winds, we follow the particle trajectories. Upon this, we derive the nucleosynthetic yields of heavy elements in the outflows, and we map the regions of Lanthanide rich and poor ejecta.

Results. We find that the outflow carries high mass of neutron rich material expanding with mildly relativistic velocities. Our accretion disks operating under the SANE mode can power the GRB jets via neutrino annihilation, if the disk to BH mass ratio is larger than about 0.01 and the black hole is fastly spinning. Slowly spinning black holes surrounded by massive post-merger disks can power these jets as well, and also be the sites of efficient nucleosynthesis of Lanthanides, responsible for the red or purple kilonova components. The long duration GRBs are potentially produced by specific type of merger events with an eccentric orbit, but in this case, their Lanthanide fraction is reduced, and the GRB luminosity due to neutrinos is also weak. We found that none of the weakly magnetized post-merger models considered here can be representative to explain the bright kilonovae associated with long GRBs like 211211A

Key words. accretion, accretion disks, gamma ray bursts, magnetohydrodynamics

### 1. Introduction

Gamma-ray bursts (GRBs) are a sudden release of about  $10^{51} - 10^{54}$  erg of energy in a volume with a radius of less than 100 km, which last from 0.01 to 100 s (for reviews, see e.g. Piran (2004); Kumar & Zhang (2015)). According to the duration time  $T_{90}$ , which is defined as the time interval over which 90% of the total background-subtracted counts are observed, GRBs are usually separated into two classes: long GRBs (LGRBs;  $T_{90} > 2s$ ), whose existence emanates from the core collapse of massive stars (Woosley 1993; Hjorth et al. 2003), and short GRBs (SGRBs;  $T_{90} < 2s$ ), whose origins are thought to be the coalescence of binary neutron stars (BNS) or neutron star-black hole (BHNS) binary systems (Eichler et al. 1989; Narayan et al. 1992).

Most of the observed GRBs (70%) have a duration of greater than two seconds and are classified as LGRBs. Since these events constitute the majority of the population, and as they tend to have the brightest afterglows, they have been observed in much greater detail than their short counterparts. Almost every well-studied long GRB has been linked to a galaxy with rapid star formation, and in many cases to a CCSN as well (Woosley &

Heger 2006). Long GRB afterglow observations which reflect their association with high redshift ( $\gtrsim 5$ ), are also consistent with the GRB having originated in star forming regions (Pontzen et al. 2010). The leading hypothesis for the short GRB origin is that they result from the mergers of compact binary systems, such as two neutron stars. The theory has been supported by the detection of gravitational waves from a neutron star merger (GW170817) coinciding with a short GRB (Abbott et al. 2017a). Their environments are diverse. Some short GRBs originate in older, elliptical galaxies with little or no current star formation, indicating that their progenitors can have long lifetimes before merging (Berger 2011). However, the majority of these GRBs are found in star forming galaxies, which differ from the hosts of long duration events. They typically have lower star formation rates and higher metallicities, resembling the general field galaxy population. In addition, short GRBs occur often at significant offsets from the centers of their hosts, sometimes even in the galactic halos. This distribution aligns with predictions of neutron star merger rates, as the neutron stars can receive 'kicks' during their formation, propelling them far away from their birthplaces (see e.g., Vigna-Gómez et al. (2018); Giacobbo & Mapelli (2018)). A wide range of progenitor ages, indicated by diversity of spatial distribution, suggests that the time between

<sup>\*</sup> agnes@cft.edu.pl

formation of the progenitor system and the ultimate merger can vary significantly, from millions to billions of years (Fong et al. 2022).

Compact binary mergers can eject large amounts of neutronrich material, which are sites of r-process nucleosynthesis and formation of heavy elements (Lattimer & Schramm 1974). The ejecta are then source of radiation emitted by the radioactive decay of the unstable heavy isotopes, which powers an Optical-Infrared transient called kilonova. As already predicted by Li & Paczyński (1998), the tremendous amount of energy along with heavy elements is emitted in an explosive outflow. Elements such as Gold or Platinum are produced in r-process nucleosynthesis, which requires extremely high neutron densities.

The elemental composition in Earth and the Solar system is driving now more interest towards fundamental questions of nuclear astrophysics(Arcones & Thielemann 2023). The Solar system abundance pattern has been identified to be a result of multiple generations of stellar nucleosyntheses. The considerable amount of <sup>60</sup>Fe (half life ~2.6 Myr) from deep ocean and lunar samples was identified as a result of likely multiple supernova explosions within ~100 parsecs over the last 10 million years. Supernova deposition is also mainly responsible for synthesizing elements slightly beyond Iron, like <sup>56</sup>Ni, which later decayed to <sup>56</sup>Fe, which is one of the dominant elements of planetary cores in the Solar system. In addition, traces the heaviest elements, including Lanthanides and Actinides like Thorium, Uranium, and Plutonium are found in the Earth. These elements are produced dominantly in compact binary mergers and (less frequently) in rare magneto-rotational (Nishimura et al. 2015; Reichert et al. 2022) or collapsar-type supernovae. The presence of a small amount of <sup>244</sup>Pu on Earth suggests that a kilonova event might have happened in the last ~100 Myrs in the close vicinity of the Solar system (Wang et al. 2021).

One of the first suspected kilonova events was the gamma ray burst GRB 130603B detected by the Swift and HST telescopes. It was a short event, lasting less than 2 seconds, with a faint, red afterglow observed several days after the initial burst. The emission was however far brighter and more persistent than expected for a typical GRB afterglow (Tanvir et al. 2013). Its red color and lightcurve slope were attributed to the radioactive decay of newly synthesized heavy elements (Berger et al. 2013). The observation was hence indicating a binary neutron star merger environment. The first confirmed GRB associated with a kilonova was observed only in 2017 (Cowperthwaite et al. 2017). The kilonova light faded away over couple of weeks, making it shorter-lived than any supernova. The spectrum exhibited evolution from blue (hot) to red (cooler) color (Abbott et al. 2017b).

The source detected in 2021, was a kilonova associated with a long GRB 211211A. It is interpreted as a merger between an NS of about 1.23 Solar mass with a BH of 8.21 Solar mass, with an aligned spin of 0.62. The data seem to be supporting an NS-first-born NS-BH formation channel (Zhu et al. 2022). The potential re-brightening of emission is in this case possibly impacted by late-time fallback accretion, while the ejected material is significantly more massive than in other types of progenitors (at least  $10^{-3} M_{\odot}$ ). As an alternative to this scenario, some authors propose however an NS-WD merger (Yang et al. 2022; Zhong et al. 2023), where the toroidal magnetic field of the neutron star is amplified by accretion of material from the white dwarf, that leads to prompt GRB emission, while the extended phase occurs during the propeller regime (Gao et al. 2022). Kilonova is here powered by the decay of Ni-56 in the debris ejecta from the WD.

Furthermore, GRB 230307A is the second-brightest long-duration GRB ever detected, and it also exhibits a rare association with a kilonova. Theoretical interpretations of this event range from a compact binary merger (Levan et al. 2024; Liu et al. 2025) to alternative scenarios involving a collapsar (Ristić et al. 2025) or a NS- WD merger with a long-lived magnetar engine (Wang et al. 2024; Arunachalam et al. 2025). Still, a possibility of kilonova originating from a collapsing massive star, that would have angular momentum slightly less that a typical long GRB progenitor, was discussed (Siegel et al. 2019). The r-process enriched collapsar model was used to fit the lightcurves of GRB 2011211A, albeit they exhibited high degeneracies among the parameters and required exceptionally high velocities of ejecta (Barnes & Metzger 2023).

In this work, we explore the scenario of a kilonova driven by NS-NS and NS-BH mergers. In particular, we study the range of energetics and durations of the events, and properties of dynamical ejecta launched from the post-merger accretion disk. We also investigate possible formation of delayed accretion episodes, which might be of particular impact to sustain the jet in a long duration GRB, launched after the compact binary merger.

Our methodology is based on detailed numerical simulation with new version of the HARM-EOS code. The code has been developed upon our publicly available scheme HARM-COOL and is updated by adding a proper 3-parameter equation of state (EOS) and a neutrino leakage module. This is aimed to represent correctly the influence of chemical evolution on the engine properties as well as account for the neutrino viscosity. We introduce the presence of a poloidal magnetic field component in the accretion flow, and we study the influence of its strength on the magneto-rotational instability. We perform both 2D and 3D numerical simulations for a period of time sufficiently long to launch enough amount of dynamical ejecta.

The article is organized as follows. In Section 2, we describe the model and setup of our numerical simulations. In Section 3, we present our calculations, describing the initial conditions, time evolution of black hole torus systems and the results of r-process nucleosynthesis calculations. We discuss our results in Section 4, and give summary and conclusions in Sect. 5.

#### 2. Numerical model

#### 2.1. Basic equations

We use the developed version of general relativistic magnetohydrodynamic code, based on High Accuracy Relativistic Magnetohydrodynamics (HARM), which has evolved from the code made publicly available by Gammie et al. (2003) and described in detail by Noble et al. (2006). Code introduces a conservative, shock-capturing scheme with low numerical viscosity, to solve the hyperbolic system of the partial differential equations of GR MHD. The numerical scheme uses the plasma energy-momentum tensor,  $T^{\mu\nu}$ , with contributions from matter (gas) and electromagnetic field. For the GR MHD evolution, we solve two fundamental equations: the equation of mass and angular momentum conservation, and energy equation.

$$T_{(m)}^{\mu\nu} = \rho h u^{\mu} u^{\nu} + p g^{\mu\nu} \tag{1}$$

$$T^{\mu\nu}_{(em)} = b^k b_k h u^\mu u^\nu + \frac{1}{2} b^k b_k g^{\mu\nu} - b^\mu b^\nu \tag{2}$$

$$T^{\mu\nu} = T^{\mu\nu}_{(m)} + T^{\mu\nu}_{(em)} \tag{3}$$

where  $u^{\mu}$  denotes the four-velocity of gas,  $b^{\mu}$  are magnetic four-vector and h is the fluid specific enthalpy. The continuity and energy-momentum conservation equations are as follows

$$(\rho u^{\mu})_{;\mu} = 0 \tag{4}$$

$$T^{\mu}_{\nu;\mu} = Qu_{\nu} \tag{5}$$

where Q is the energy change per unit volume due to neutrino cooling. Finally, the Maxwell equations in the limit of ideal MHD read

$$F^{\mu\nu}_{;\mu} = 0,$$
 (6)

with the  $F^{\mu\nu}$  being the electromagnetic (Faraday) tensor.

The GR MHD are brought in conservative form, by implementing a Harten-Lax-van Leer (HLL) solver <sup>1</sup>(Harten 1983) to calculate numerically the corresponding fluxes.

For this study, we have developed a new version of our code, upon the one introduced by Janiuk (2019). The new version, named now HARM\_EOS, is supplied with a new scheme for the simulation of a post-merger accretion disk evolution with detailed microphysics. It works with a tabulated, three-parameter equation of state of dense matter and accounts for the neutrino cooling/heating, via a leakage scheme.

We note that in the continuity equation, 4, the conserved quantity is the baryon density,  $\rho = m_b n_b$ . The lepton density is changing due to weak interactions, and is given by the net rate of neutrino and antineutrino number density,  $\mathcal{R}$ , as:

$$(\rho Y_e u^\mu);_\mu = \mathcal{R}. \tag{7}$$

Here  $Y_e = n_e/n_b = m_b n_e/\rho$  is the electron fraction.

With this additional constraint, the numerical scheme must solve the system of GR MHD equations in a conservative form and required rebuilding of the inversion scheme to recover conserved variables. The details of recovery methods tested and used in our code, and the neutrino treatment details, are presented in Appendices A and B the end of the article.

To probe the accretion disk outflows, we use the tracer particle method, the same as implemented in Janiuk (2019). The particles are initialized in the densest parts of the initial accretion disk, and store in time the information about the outflow physical properties.

Below, we discuss the initial conditions in models evolved by our numerical scheme, and then we show results of numerical simulation, addressed to the post-merger system after the coalescence of binary neutron stars, or a neutron star with a stellar mass black hole. We find that the plasma is very neutron-rich, so the r-process nucleosynthesis in the ejected material may lead to unstable heavy isotopes creation, responsible for a kilonova.

Our simulations are performed in the axisymmetric 2D setup, and some chosen models are also run in 3D. The resolution is of  $256 \times 256 \times 1$  and  $256 \times 256 \times 64$ , in radial, polar, and azimuthal directions, respectively. The ejecta from post-merger accretion

disk are analyzed with the test particles (tracers), to determine the mass and composition of the kilonova powering material. We then study nucleosynthesis of heavy elements in the postmerger winds, via postprocessing of the tracer results. In one of the 3D runs, we also address a non-axisymmetric perturbation in the initial distribution of internal energy inside the torus, imposed at 0.4%.

#### 2.2. Initialisation of the run

We start our simulations from the pressure equilibrium configuration of a rotating torus around a Kerr black hole. We solve for its structure given the specific enthalpy, h, resulting from the FM torus angular momentum solution l, given by Fishbone & Moncrief (1976). We find the distribution of density and temperature in the disk by Newton-Raphson method, which minimizes the condition for  $h=1+P/\rho+u/\rho$ , where P and u are pressure and internal energy found in the Helmholtz EOS tables (Timmes & Swesty 2000). The fixed parameters are the entropy and electron fraction in the disk,  $S_{disk}$  and  $Y_{e,disk}$ .

Our initial torus extends from the cusp radius,  $r_{in}$ , and the radius of pressure maximum,  $r_{max}$ , where the FM solution is determined. Outside the torus, we set the constant density and temperature conditions, as well as a constant electron fraction.

We seed the torus with the initial poloidal magnetic field. We assume the form of the magnetic vector potential given by

$$A_{\varphi} = \max \left( \frac{\bar{\rho}}{\rho_{\text{max}}} - \rho_0, \, 0 \right) \tag{8}$$

where  $\bar{\rho}$  is the density in the torus (averaged over 2 neighboring cells) and  $\rho_{\rm max}$  is the density maximum, and we use  $\rho_0=0.2$ , to restrict the initial field to the regions where the density in the torus is larger than  $0.2\rho_{\rm max}$ . Other spatial components of the initial vector potential are  $A_r=A_\theta=0$ , hence, the magnetic field will have only  $B_r$  and  $B_\theta$  components. We set the field strength by normalizing it to the chosen minimum value of gas to magnetic pressure ratio,  $\beta_{min}$ , inside the torus. Our typical value is in the range of 50-100, to ensure the initial torus is weakly magnetized.

The torus is embedded in a cool, rarefied atmosphere. We assume the atmosphere density of  $D_{atm} = 3 \times 10^{-7}$  g cm<sup>-3</sup>, that exceeds the numerical floor of density (set typically at  $10^{-5}$  in the code units and decreasing with radius as  $r^{-2}$ ), and we adopt the electron fraction in the atmosphere  $Y_{e,atm} = 0.45$ . The atmosphere temperature is then found in the EOS tables and is about  $T_{atm} = 0.002$  MeV. The floor temperature is much lower, and scales with radius as  $T_{floor} = T_0/r$ , with  $T_0 = 10^3$  K.

#### 3. Results

We explore the properties of two fiducial models of  $\sim 0.1 M_{\odot}$  and  $\sim 0.01 M_{\odot}$  torus, optically thick or thin to neutrinos, respectively, and located around a  $3 M_{\odot}$  black hole mass formed after compact binary merger. These models aim to reconstruct the outcome of a typical binary NS-NS merger scenario. We also probe the scenario of a higher mass ratio between the BH and disk mass, considering smaller remnant tori of about  $\sim 0.02 M_{\odot}$  and  $\sim 0.002 M_{\odot}$ , for the optically thick and thin case, respectively. These models are aimed at reconstructing a BH-NS merger scenario to find out quantitative differences in the nucleosynthesis patterns between the two merger types. Finally, we study a system of a  $\sim 0.8 M_{\odot}$  post-merger torus located around a 8.2  $M_{\odot}$  black hole, as motivated by the recently observed kilonovae and

<sup>&</sup>lt;sup>1</sup> It is an approximate Riemann solver. Generally speaking, Riemann solvers are specific methods for computing the numerical flux across a discontinuity in the Riemann problem (a specific initial value problem composed of a conservation equation together with piecewise constant initial data that has a single discontinuity in the domain of interest). They form an important part of high-resolution schemes in computational fluid dynamics and computational magnetohydrodynamics.

constraints on their progenitor parameters. Therefore, while for fiducial models we assume a typical highly spinning black hole,  $a \sim 0.9$ , for the latter, massive one, we adopt a moderate black hole spin value,  $a \sim 0.6$ .

Parameters of the fiducial model are BH mass of  $3M_{\odot}$ , and its dimensionless spin a=0.9375. The initial gas-to-magnetic pressure ratio  $\beta$  is normalized to the minimum value inside the pressure maximum radius,  $r_{max}$ . The inner disk radius is initially located at  $r_{in}=4r_g$ . The disk mass is about  $0.01-0.1M_{\odot}$ , adopted for an optically thick and optically thin model, respectively. The optical thickness of the torus is regulated by the choice of entropy per baryon,  $S_{disk}$ , as the values of density and temperature in the torus are found in EOS tables for a given entropy, electron fraction, and specific enthalpy profile. To do that, we must prescribe the initial chemical composition of the torus, with a constant electron fraction chosen as  $Y_e=0.1$ . The values of entropy per baryon are either S=10 (for optically thin case) or S=7 (for thin case).

Apart from the fiducial models, we also run test models with smaller disk masses, about  $0.02-0.002 M_{\odot}$ . Finally, we simulate the case with parameters tuned to the central engine of the 'kilonova' event GRB 211211A, where the black hole spin and mass ratio estimates were obtained from observations. Also, to test whether this 'kilonova' scenario can represent a long duration GRB event, we modify the initial condition to account for an eccentric merger. This is done by introducing a non-axisymmetric perturbation in the energy distribution.

Parameters and final times of all runs are given in Table 1.

#### 3.1. Time-dependent evolution

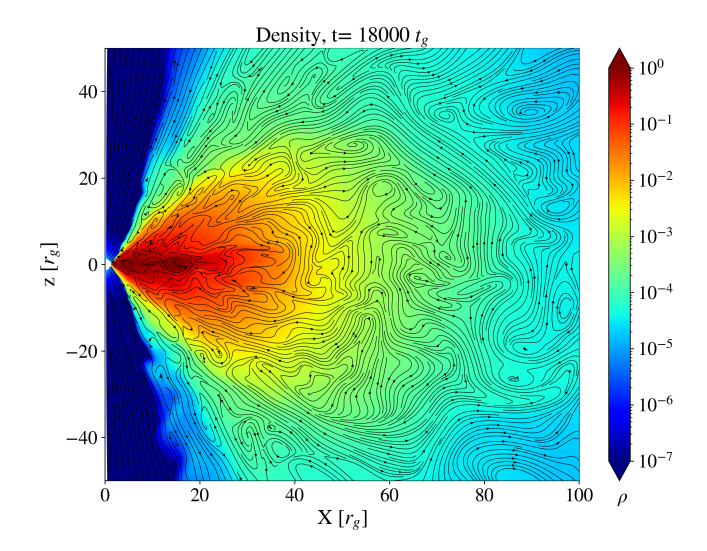
#### 3.1.1. Fiducial thin and thick models

In Figure 1 we show the snapshot of a fiducial 2D simulation. The model shown is 2D-Thin, and the maps are taken at time  $t = 18000t_g$  Polar plots are showing the distribution of density (in code units, top panel) with overplotted magnetic field lines. Maps of other quantities from the same simulation are shown in Figure 2, see below.

The dense and almost completely neutronized material is located near the equatorial plane of the disk. At intermediate latitudes, the disk launches fast, magnetically driven and neutrino cooled outflows. We estimated their velocities to be  $v/c \sim 0.11-0.23$ . These outflows are launched with a broad range of electron fraction  $Y_e \sim 0.1-0.45$ . The details of mass loss and thermodynamic properties of winds are sensitive to engine parameters: BH spin and magnetization of the disk, as shown before by Janiuk (2019); Nouri et al. (2023). In general, more magnetized disks should produce faster outflows. The winds will eventually contribute to the kilonova signal, due to radioactive decay of r-process formed isotopes, and this nucleosynthesis site is complementary to the dynamical ejecta launched prior to the compact binary merger.

In Figure 2, we plot the neutrino emissivity and optical depth color maps for the same model and snapshot as shown in Fig. 1. The simulation aimed to produce an optically thin model, and in fact, the  $\tau>1$  region is limited to the narrow strip at the equatorial plane, where also neutrino emissivity is largest. Otherwise, the medium is always optically thin with  $\tau<1$ , for both scattering and absorptive processes.

For other 2D models, we note that qualitatively, they follow a similar pattern in evolution. The quantitative difference between thin and thick scenarios is that the latter results in a much denser torus and much lower electron fractions, located near the equato-



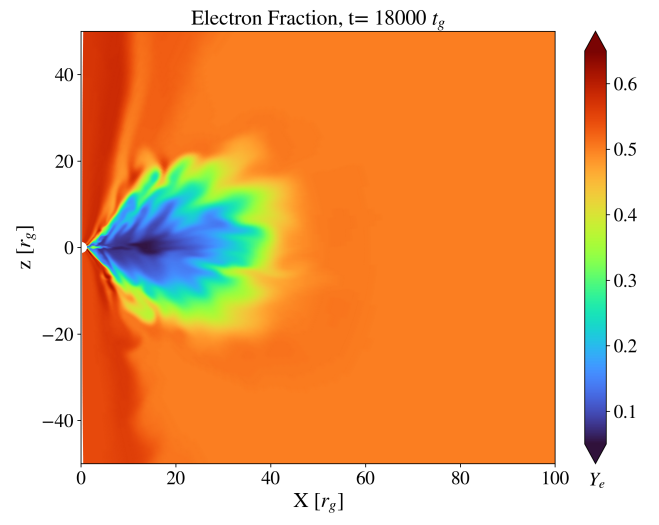


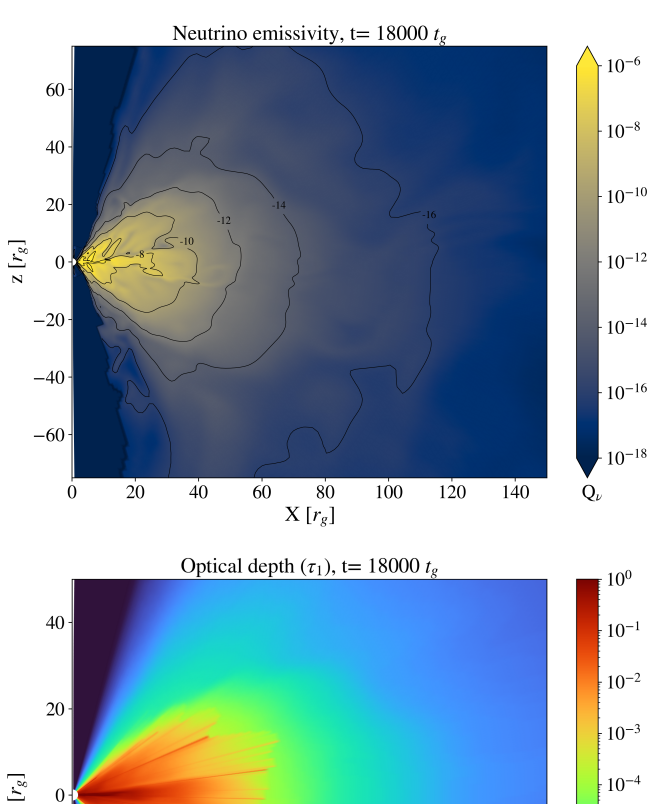
Fig. 1 Snapshots from the 2D simulation of the GRB central engine from model 2D-Thin. The top panel shows the density and magnetic field streamlines distribution in the innermost part of the accretion disk. The bottom panel shows its chemical composition parameter - the electron fraction. Snapshots are taken at time  $t=18000\ t_g$ 

rial plane. Most of this neutron rich material is however accreted with the inflow of matter, while the neutronisation of unbound winds are similar. Some quantitative differences in the distribution of  $Y_e$  will lead to different heavy elements abundance patterns after nucleosynthesis, which will be presented in the next Section. The difference in distribution of neutrino emissivities is such that the thick models are brighter in neutrinos in their central parts, while the thin models are bright mostly at the disk surface. At the evolved state, the total neutrino luminosities differ by about factor of 5-8, see below.

The neutrino emissivities integrated over the volume give the total neutrino luminosity of the disk and outflows. We plot this quantity as a function of time, for the 2D models, in Figure 3. Neutrinos of three flavours are shown, and the luminosity in electron and anti-electron neutrinos is not equal, but it is much higher than in other heavy lepton neutrinos. We do not consider here neutrino oscillations, so the latter flavor is found energetically negligible (see however Nagakura et al. (2025) for recent results on neutrino oscillation effect).

Table	1 Models and	their narg	meters in	the nume	rical cim	ulatione
rame	i wiodeis am	i uien bara	uneters in	the nume	ancai siiii	uiauons

Model	resolution	$r_{in}$	$r_{max}$	β	а	$M_{BH}$	$M_{disk}$	$S_{disk}$	$N_{tr}(t_0)$	$N_{tr}^{out}(t_f)$	$t_f$
2D-thick-s	288x256x1	4.0	9.0	100	0.9375	3.0	0.021	7	11072	186	20,000
2D-thin-s	288x256x1	4.0	9.0	50	0.9375	3.0	0.002	10	11049	372	20,000
2D-thick	288x256x1	4.0	9.78	100	0.9375	3.0	0.129	7	15998	1037	20,000
2D-thin	288x256x1	4.0	9.78	50	0.9375	3.0	0.013	10	15988	554	18,200
2D-kn	288x256x1	4.0	12.6	50	0.6	8.2	0.785	10	20392	931	20,000
3D-thick	256x128x64	4.0	9.78	100	0.9375	3.0	0.129	7	8131	1063	19,800
3D-thin	256x128x64	4.0	9.78	50	0.9375	3.0	0.013	10	8124	544	18,300
3D-kn	288x128x64	4.0	12.6	50	0.6	8.2	0.781	10	10344	1000	20,000
3D-kn-p	288x128x64	4.0	12.6	50	0.6	8.2	0.834	10	9954	281	20,000



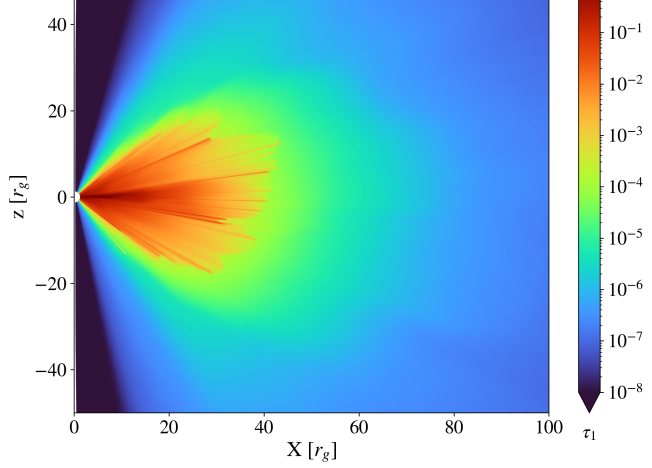


Fig. 2 Snapshots from the same 2D simulation of the short GRB central engine, as shown in Fig.1. Here, the top panel shows the neutrino cooling rate in the innermost part of the accretion disk. The bottom panel shows the color map of neutrino optical depth.

We highlight here the comparison between thin and thick models total luminosities, in addition to the test models with small disk masses, denoted as 2D-Thin-s and 2D-Thick-s. The optically thin models have  $L_{\nu} \sim 10^{52}$  erg/s at the initial time, and slowly decrease by about one order of magnitude within the simulation time of 300 ms. This value is clearly related to the

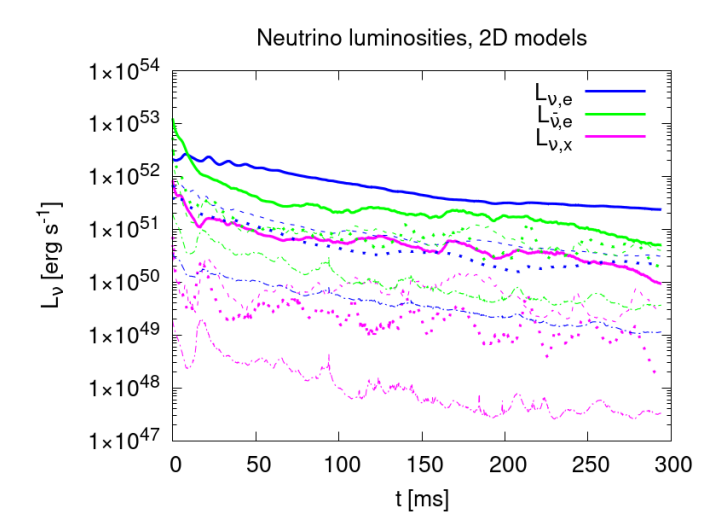


Fig. 3 Neutrino lightcurves for the 2D models, optically thin and thick disk Plots show 2D-Thin-s and 2D-Thin models, with thin dot-dashed and dashed lines, respectively, and 2D-Thick-s and 2D-Thick models, with thicker dotted and solid lines, respectively. Three colors, blue, green, and magenta, represent luminosities in electron neutrinos, electron anti-neutrinos, and heavy lepton neutrinos, respectively.

initial mass of the disk, being  $0.013~M_{\odot}$  and it is about an order of magnitude lower for the test model with a small disk mass of only  $0.002~M_{\odot}$ . These models have the same global parameters (black hole spin, magnetic field strength), so we expect that the luminosity of the jet driven by the black hole rotation mediated by magnetic fields (i.e., the Blandford-Znajek process) would be the same. However, neutrinos may be a much weaker source of jet power in the case of a small mass of the disk (i.e., disk to black hole mass ratio). We notice, that at late time of evolution, the slope of neutrino lightcurve for test model becomes flat, so the difference in neutrino-power may not be significant at later times

The thick models are brighter in neutrinos, by more than order of magnitude, and luminosity  $L_{\nu} \leq 10^{53}$  erg/s is related to a large mass of the disk, which is about 0.13  $M_{\odot}$ . The initial difference between electron and anti-electron neutrino luminosities is due to larger absorption for  $L_{\nu,\bar{e}}$ . The  $L_{\nu,x}$  in the simulation stays order of magnitude lower.

The models with small disk mass evolve with a similar slope of the neutrino luminosity as the fiducial models. We speculate that in neutrino thick cases, the jet powered by neutrino annihilation will be launched successfully from the central engine,

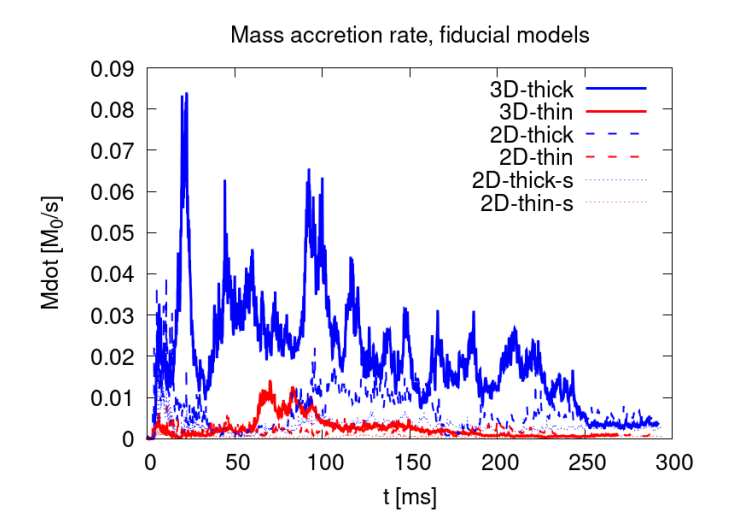


Fig. 4 Mass accretion rates for Thin and Thick models. The 2D-Thin-s, 2D-Thin and 3D-Thin models are shown in red, with dotted, dashed and solid lines, respectively. The 2D-Thick-s, 2D-Thick and 3D-Thin models are shown in blue, with dotted, dashed and solid lines, respectively.

even though its magnetization is less, and the BZ power might be insufficient to sustain the jet.

We note here that in all 2D models, the accretion disk operates under the SANE (standard and normal) accretion mode. The so called MAD, magnetically arrested state, would be reached if the normalized magnetic flux on the black hole horizon,  $\phi_{BH} = 1/(2\sqrt{m})\int_{r_{hor}} |B^r| \sqrt{-g}d\theta d\phi$ , satisfies the condition of minimum value around  $\sim 15$  (for the code using Gaussian units). In our 2D models, it is never larger than 10, albeit varying over time, according to the accretion rate variations (see below). In all fiducial models, we get  $\phi_{BH} \sim 1-4$  for most of the simulation time, regardless of the dimensionality of the run.

The effects of 3D simulation on the density distribution are seen mostly in the accretion rate. In Figure 4 we compare the accretion rate at the black hole horizon radius, as a function of time, for optically thin and thick scenarios, modeled with either 2D or 3D Setups. The 3D-Thick simulation results in 2-3 times higher accretion rate than for its 2D counterpart. For the 3D-Thin simulation, the mean accretion rate is smaller, and at late times it is similar to that in the 2D model. As will be shown in the next Section, the difference is also found in the mass outflow rates. We attribute this effect to the magnetic turbulence and enhanced transport of angular momentum by magnetic fields, in case of the full 3D setup.

The magnetic flux on the BH horizon, in 3D models, has similar values as in the 2D cases. For the 3D-Thin run, it stays about  $\phi_{BH} = 2 - 3$  for most time, and it is increasing up to about  $\sim 5$  at the end of the run. For the 3D-Thick run, the value is always between  $\phi_{BH} = 1 - 2$ .

#### 3.1.2. Kilonova central engine models

In addition to our thin and thick models, we also performed calculations with central engine parameters tuned to represent kilonova sources. In particular, we aim to test a scenario for GRB 211211A. The engine parameters mimic the compact binary mass ratio, and final black hole spin after the merger. The models 2D-kn, 3D-kn, and 3D-kn-p were run until final time

of  $20,000 \, t_g$ . In one of the 3D models, we allowed for a non-axisymmetric perturbation of the internal energy while initializing the simulation. We aimed to reproduce the physical properties of the system, prolong the activity time, and further discuss the implications for heavy element nucleosynthesis. In this way, we want to verify whether compact binary merger scenario is plausible for this source, among other ideas recently proposed in the literature.

In Figure 5 and 6 we present polar slices of the 3D models. Their top panels present density and velocity field distribution, while the bottom panels show magnetisation in the flow. Figure 5 shows model 3D-kn initialized in an axisymmetric setup, while in Fig 6 we show scalar and vector fields for the 3D-kn-p model, with initial perturbation. One can notice quantitative differences between the two models, at the evolved state of  $t = 18,000 t_a$ . Clearly, the low density funnel becomes wider in the case of the perturbed model, which translates into a larger potential jet opening angle. Simultaneously, the accreting torus is denser and more compact within the innermost  $\sim 30 r_g$ , in the 3D-kn-p model. The magnetisation profiles reveal different shapes of turbulent regions inside the torus, as well as in the surface layers where the winds are launched. The winds from the perturbed model are less dense and distributed more towards the equatorial plane than the winds from the unperturbed scenario. The mass loss and other properties of the winds, affecting subsequent nucleosynthesis patterns, are also different (they will be discussed in the next Section).

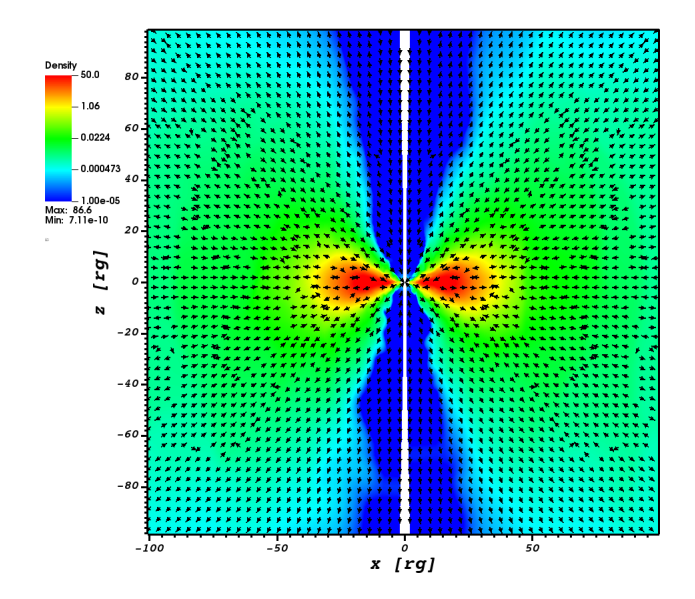
At this point, we only highlight the fact that the 2D-kn and 3D-kn models are quantitatively similar in terms of torus structure, mass loss, and also neutrino luminosity, as shown in Fig. 7. Here, the dashed and thick solid lines practically overlap within the first  $\sim 300$  ms, for all neutrino flavors. The azimuthally perturbed model, 3D-kn-p, exhibits a lower neutrino luminosity than the axisymmetric one and it is declining at a somewhat faster rate. The average electron neutrino luminosity found in our simulations is about  $2.3 \times 10^{51}$  erg s<sup>-1</sup>, and  $1.1 \times 10^{51}$  erg s<sup>-1</sup>, for the 3D-kn and 3D-kn-p models, respectively. Noting that according to recent estimates, the neutrino annihilation efficiency is about  $\sim 0.1 - 1\%$  (Du et al. 2019), we speculate that it is a small  $L_{\nu}$ , and this engine is not able to power a bright GRB jet for a long time.

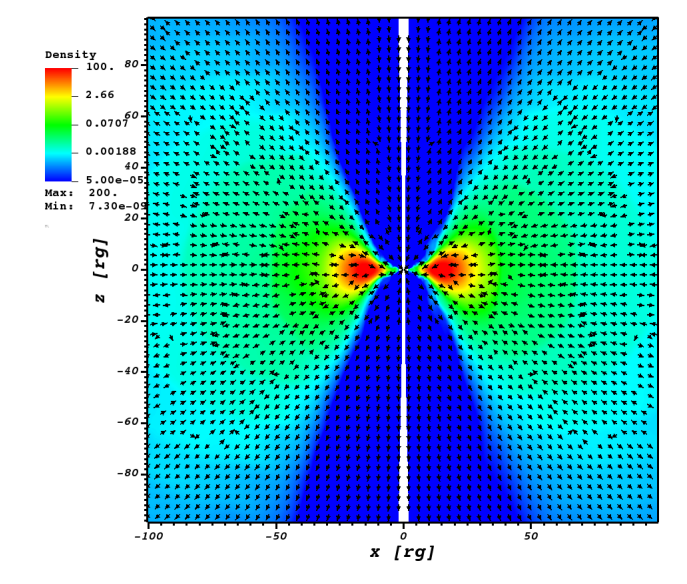
In Figure 8 we show the mass accretion rate at the black hole horizon, for the 2D-kn, 3D-kn and 3D-kn-p models. The accretion rate in 2D and 3D simulations is comparably large, and it is also an order of magnitude larger than in the above presented fiducial models. The engine lifetime is hence longer, and accreting tours will be able to power the GRB and kilonova for a longer time, launching powerful winds. The non-axisymmetric perturbed model, 3D-kn-p, presents however, a negligible accretion rate for most of the simulation. The magnetic field is also not transported towards the horizon, and as discussed above, the neutrino luminosity of this model is also small. We conclude that in this scenario, the jet will not have any source of power, neither from neutrinos nor the Blandford-Znajek mechanism. The system will then end up as a failed jet, with possible orphan kilonova emission from unbound winds.

Below, in the next Section, we quantify the properties of these winds and the resulting nucleosynthetic patterns in all our scenarios.

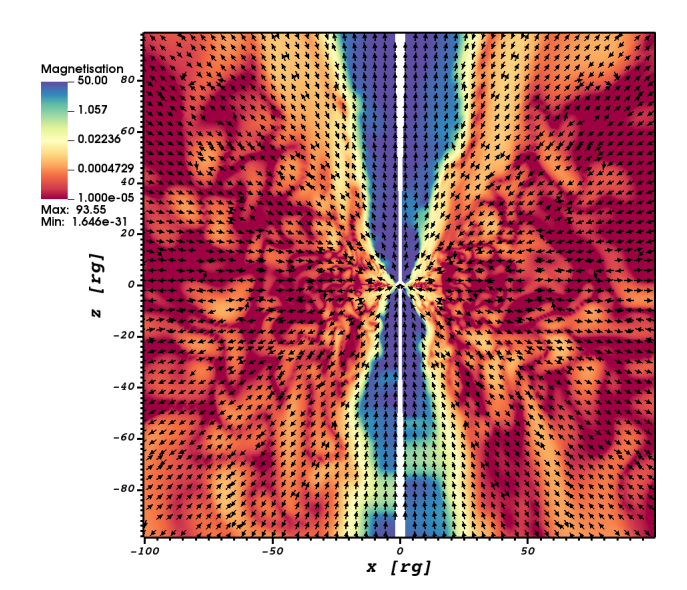
## 3.2. Mass loss in the outflows from accretion disk

In general, outflows are launched in all simulations; however, their properties differ. To quantify the outflows, we first measure

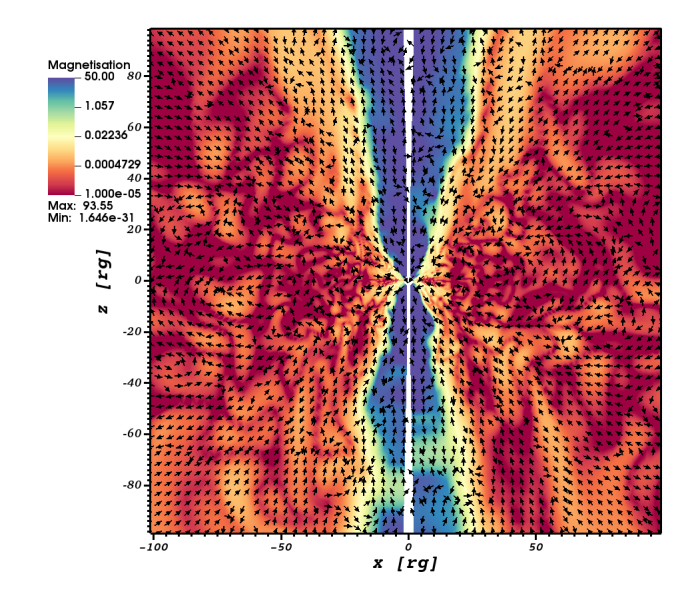




Time = 18000



Time = 18000



Time = 18000

Fig. 5 Distributions of density  $\rho$  (code units) with superimposed velocity field, and magnetisation,  $\sigma = B^2/\rho$  and magnetic field vector fields, at time t=18000  $t_g$  for the 3D 'kilonova' model 3D-kn.

the mass flux integrated over the surface of the outer boundary. This quantity gives us a cumulative mass of the outflows as a function of time. The results for 2D simulations are shown in Fig. 9. We notice that the largest mass of the outflow,  $\sim 0.0045$  Solar mass, was produced by the 2D-Thick model, which had the largest initial mass. However, the ratio between the ejected mass and initial disk mass is here only about 3.5%. The 2D-Thin model, and both the 2D-Thin-s and 2D-Thick-s models did not reach the state where the mass outflow saturates at a constant value. It can first increase linearly, but presumably later it will rather saturate at a constant value, when the simulation would reach a steady-state. Nevertheless, at the final time of this simulation, the mass lost by the torus in 2D-Thin model is already about 11% of its initial mass  $(0.0015 \text{ vs. } 0.013 M_{\odot})$ . The opti-

Time = 18000

Fig. 6 Distributions of density,  $\rho$  (code units) with superimposed velocity field, and magnetisation,  $\sigma = B^2/\rho$  and magnetic field vector fields, at time t=18000  $t_g$  for the 3D 'kilonova' model, with non-axisymmetric perturbation 3D-kn-p

cally thin model is therefore more prone to the efficient launching of winds from the accretion disk.

Next, we check whether the mass outflow rate depends on the dimensionality of the simulation. In Figure 10 we show comparison of the mass outflow rates from the 3D-kn and 2D-kn models. They are very similar, and reach about  $0.1~M_{\odot}$  at the end of the simulations. Relatively, the value of the outflow mass is about 12% of the initial mass of the torus. The dimensionality does not affects results, as was already shown by the neutrino luminosities. However, for the model with perturbation, the mass outflow rate is almost 100 times less, than in the unperturbed model, for the same initial disk mass. It is actually comparable to the small mass in 3D-kn-thin model, which was axisymmetric, but had more than 50 times less initial mass of the torus.

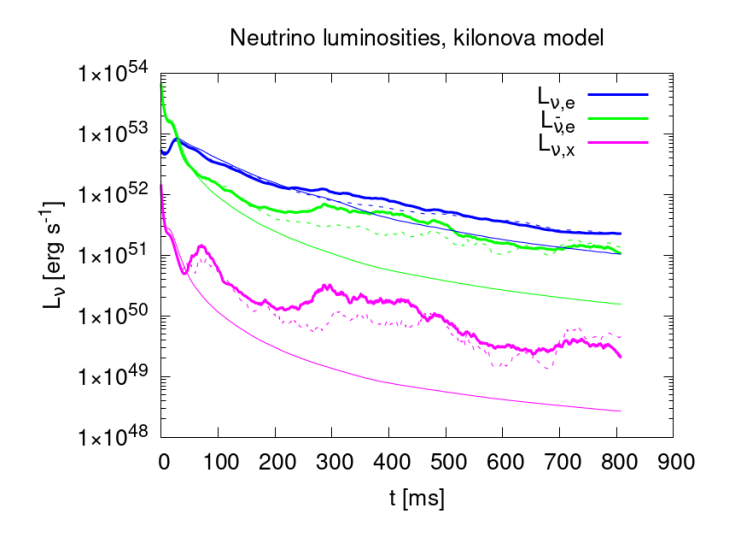


Fig. 7 Neutrino lightcurves for our kilonova scenario. The 2D-kn and 3D-kn models are shown, with dashed and solid lines, respectively. In addition, we show the results for the 3D-kn-p model, with a thinner solid line. Colors of the lines represent various neutrino flavors, same as in Fig. 3.

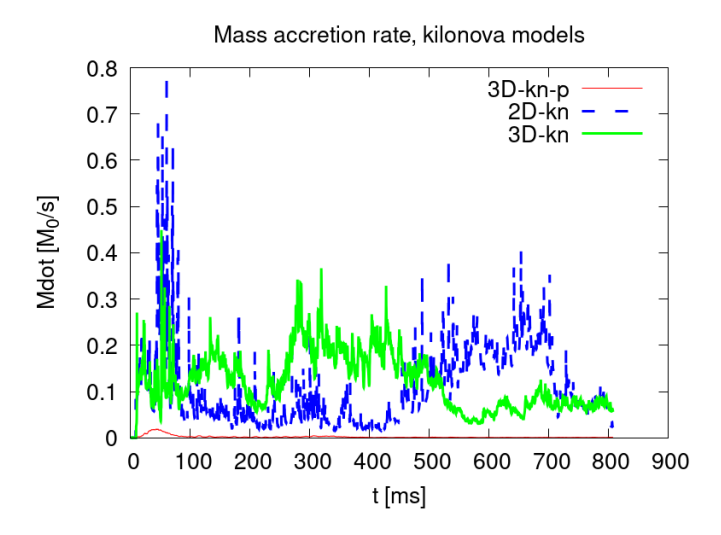


Fig. 8 Mass accretion rate in kilonova scenario. The 2D-kn and 3D-kn models are shown, with blue and green lines, respectively. In addition, we show the results for 3D-kn-p model, with a thinner red line.

This shows, that eccentric models, studied here via perturbing the initial structure of the torus, the flow appears more bound. Our estimations will be further quantified via the tracer particles analysis in Sect. 3.2.1.

In Figure 11 we show visualisation of the 3D axisymmetric kilonova engine, model 3D-kn. The snapshot shows distribution of density within the volume of inner 100  $r_g$  region, and corresponding velocity field. Clearly, powerful wind outflow is launched from the accretion disk.

### 3.2.1. Evolution of outflows probed by tracer particles

To analyze disk outflows, we employ the tracer particle technique, as originally introduced in Janiuk (2019) for the HARM\_COOL code. Tracer particles record properties of the

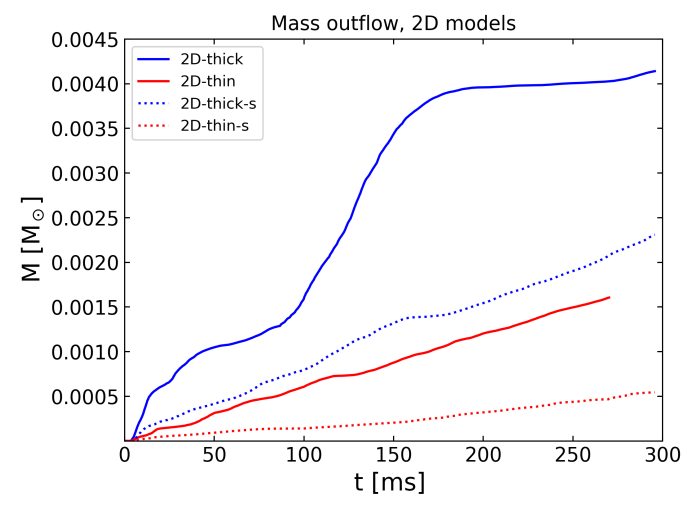


Fig. 9 Cumulative mass outflow from the outer boundary, for the 2D models.

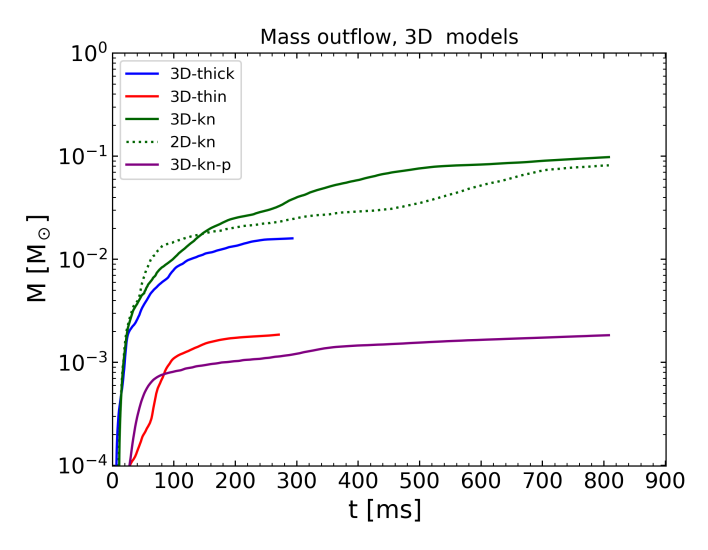


Fig. 10 Cumulative mass outflow from the outer boundary, for the 3D models. Notice the logarithmic scale used in this plot that cover several order of magnitude. Note the time expressed in physical units is different for fiducial and 'kn' models, because of different  $t_g$ , while all models were evolved over the same time in code units.

flow, such as density, temperature, and electron fraction in the disk winds escaping through the outer boundary of the computational grid. In Figure 12 we visualize the subset of particles, ejected in all our 3D simulations, showing in each panel a 3D Cartesian box with coordinates scaled logarithmically and normalized in gravitational radius units,  $r_g$ . Each color represents a specific time interval over which the outflow parcel is reaching the outer boundary. In top panels, we show the 3D-kn and 3D-knp models. One can notice that the trajectories in perturbed model are mostly cycling around the black hole, while only a small subset of particles is leaving the computational box. The color coding reveals however, that these parcels are having high velocities and they escape at early time intervals. In the bottom panels, the thin and thick models, 3D-Thin and 3D-Thick, are shown. For the 3D-Thin model, we notice that even though more particles in total are leaving the box as unbound winds, their time of arrival to the outer boundary is late. These particles are slow and more

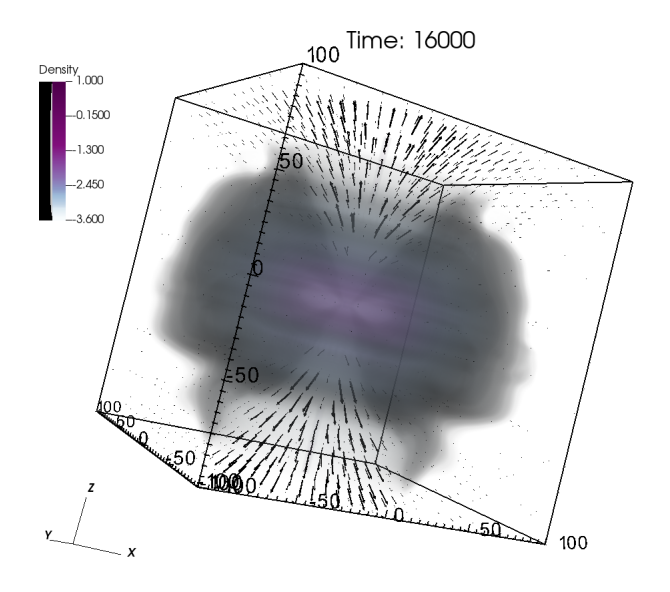


Fig. 11 Volume rendering plot of density and overimposed velocity field in the wind outflow. The plot shows axisymmetric kilonova model 3D-kn, at the final time snapshot  $t = 16,000t_g$ . Density is expressed in logarithmic scale, in code units.

massive. In consequence, even though the resulting cumulative mass loss in 3D-Thin model is very similar to the 3D-kn-p case, as shown in Fig. 10, the wind properties and its time histories are different. Also, possibly the chemical properties are different in our fiducial model cases, and in the kilonova scenario case (see below in Sect. 3.3). As for the 3D-Thick model, the outflowing particles are shown to move faster and reach outer boundary at earlier intervals, while the cumulative mass of the outflows is an order of magnitude larger than in formerly discussed models, and now similar to the 3D-kn case. The latter is possibly having heavier particles in the unbound material (their composition will be presented below in Sect. 3.3). The cumulative mass outflow is larger by a factor of a few, because the initial mass of the disk was six times larger in 3D-kn than in 3D-Thick.

# 3.3. Chemical composition and nuclear reaction network calculations

To compute r-process nucleosynthesis in the outflows of the GRB engine, we use the data from tracers, which are post processed using the nuclear reaction network. Here we use the code SkyNet (Lippuner & Roberts 2017) to simulate the nuclear reactions and evolve the abundance of nuclear species synthesized in these reactions. SkyNet incorporates both strong and weak reaction libraries, enabling the evolution of a wide range of nuclear processes, including symmetric and spontaneous fission. Energy released in the reactions is used to update the temperature self-consistently, while Coulomb screening corrections are excluded in our setup.

In Figure 13, we show the distribution of the electron fraction,  $Y_e$ , as a function of velocity, v, for all four 3D models, which are grouped by their BH mass. For each model, the entire velocity distribution is binned, and for each velocity bin, the corresponding distribution of  $Y_e$  is plotted. We show the minimum-maximum range of electron fraction with thin lines, the 25%-75% quartiles with solid boxes, and the mean values are marked

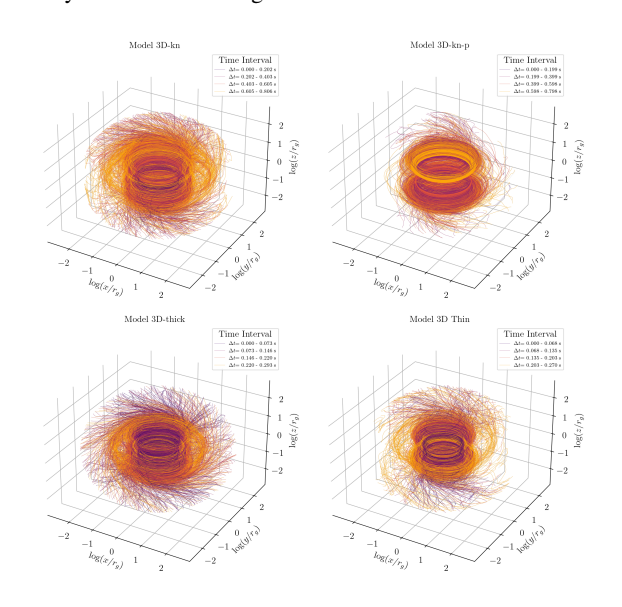


Fig. 12 Distributions of trajectories of particles sampling the outflow from central engine. Top panels show the case of 'kilonova' axisymmetric and perturbed models, while bottom panels show the fiducial models, Thin and Thick. In case of 3D-Thin model, the quantitatively similar cumulative amount of mass is leaving the box as in the perturbed 3D-kn-p model. The same holds for 3D-Thick and 3D-kn models.

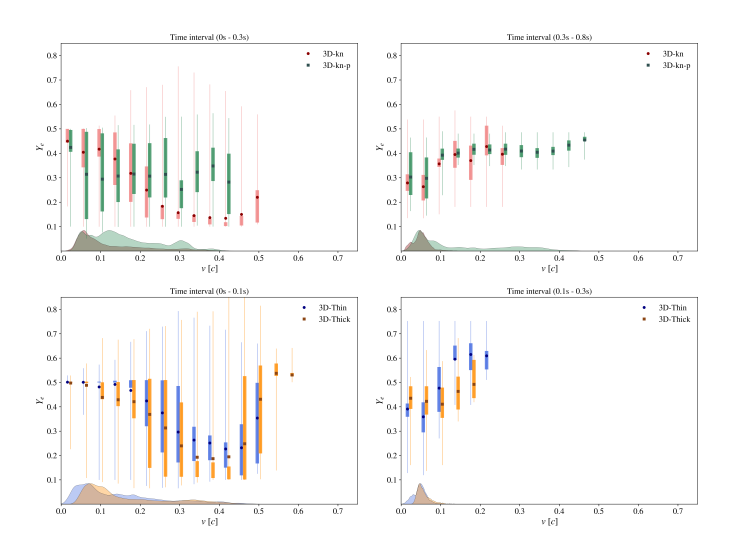


Fig. 13 Binned electron fraction ( $Y_e$ ) versus ejecta velocity ( $\nu$ ), plotted for the 3D models, the same as shown in Fig. 12. Vertical bars indicate the full range (thin lines) and interquartile range (thick bars) of  $Y_e$  values in each velocity bin, with markers denoting the mean. The bottom ribbons show the kernel density estimate (KDE) of the velocity distribution for each model. The left and the right panels show ejecta sampled at early and late periods of evolution, respectively.

as well. To illustrate the temporal evolution, we divide the simulations into early and late phases. For the 3D-Thin and 3D-Thick models (final time in physical units was 0.3 s), these intervals are 0-0.1 s and 0.1-0.3 s. For the 3D-kn and 3D-kn-p models (their final time was 0.8 s), the division is 0-0.3 s and 0.3-0.8 s. It should be noted that while the velocity is always calculated from tracers, the source of  $Y_e$  differs: for the early time analysis,  $Y_e$  is evolved directly in the HARM-EOS code, but for the late

time analysis, it is taken from the postprocessing results of the nuclear reaction network.

The temporal evolution of the disk wind reveals significant differences in outflow properties across the models. In the early phase, the ejecta are fast and compositionally inhomogeneous, characterized by a broad  $Y_e$  distribution and velocities extending beyond v = 0.5c. In the velocity range with considerable statistics (see the KDE histogram), we infer that the fastest ejecta are the most neutron-rich, representing fluid elements launched from the internal region of the accretion disk. While the 3D-Thin, 3D-Thick, and 3D-kn models show a similar evolutionary trend, it is interesting to note that the 3D-kn-p model has a more uniform distribution of  $Y_e$  across all velocities. It should also be noted that the velocity KDE for 3D-kn-p has the largest spread in the 0 - 0.4c range, suggesting its ejecta are the most dynamically variable. As the wind evolves into the later phase, two trends are observed: the composition settles towards higher  $Y_e$ values and the fluid decelerates. The wide  $Y_e$  distribution from the early phase tightens considerably, with the mean  $Y_e$  reaching  $\approx 0.4 - 0.6$  for the 3D-Thin/Thick models and  $\approx 0.3 - 0.45$  for the 3D-kn/kn-p models. The high-velocity component of the 3D-Thin/Thick wind effectively vanishes, with most late-time material slowing down below v = 0.2c. In contrast, the 3D-kn-p model maintains a more powerful outflow, with a persistent velocity tail reaching  $v \approx 0.45c$ . This suggests that the central engine of the 3D-kn/kn-p models drives a more sustained and neutron-rich wind compared to the more rapidly waning outflow of the 3D-Thin/Thick models, and also that the perturbed model results in fast outflows maintained even in late times.

#### 3.3.1. Abundance patterns and ratios of chosen elements

Post-processing was carried out on the tracers from all nine models, and the abundance profiles of isotopes from the nuclear reaction networks were generated for each model. The mean relative abundance of isotopes, extrapolated at 1 Myr for the 3D models from all the corresponding trajectories, is provided in Figure 14. Solar abundance profile (Arnould et al. 2007) is also added in the same plot for comparison. The r-process calculations were carried out for all models, with tracer particles being post-processed in SkyNet once their temperature falls below 10 GK. The composition is first evolved in nuclear statistical equilibrium (NSE), and as the temperature further drops to 7GK, the network gets switched to the standard reaction evolution. We note that different studies (Siegel & Metzger 2017; Combi & Siegel 2023) adopt varying thresholds for the onset of network evolution and for the NSE transition, typically in the range of 5–10 GK. The choice of these transition points influences the results, as the electron fraction  $Y_e$  at 5 GK is generally higher than at 10 GK, a difference that is likewise reflected in the final abundance patterns obtained from the full reaction network.

A robust production of heavy elements through r-process nucleosynthesis is evident in the resulting abundance patterns, which clearly exhibit the first, second, and third r-process peaks, along with distinct signatures of Lanthanides and Actinides. In the *3D-thin* and *3D-thick* models, the heavy element part represented by the 2nd and 3rd peak has gone considerably lower, while in the *3D-kn* and *3D-kn-p* models, this is not the case. We also notice that for all models, light elements have gotten higher in abundance when network evolution was initiated at 7 GK.

While each model shows slight variations in the relative abundances of light and heavy nuclei, the overall profiles closely reproduce the Solar abundance distribution and its characteristic r-process features. We further analyse these nucleosynthesis pat-

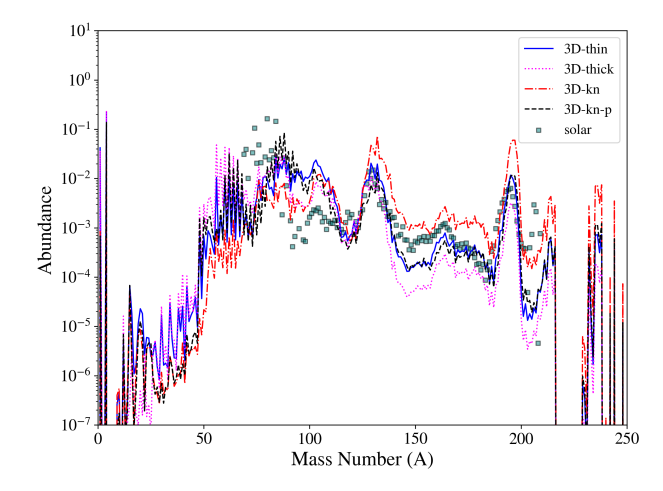


Fig. 14 Mass abundance profiles from the nuclear reaction network for all 3D models in the sample. The solar abundance profile is included for comparison.

terns by comparing the heavy to light elements ratios. Figure 14 illustrates clear differences in the nucleosynthetic yields of light and heavy r-process elements across our 3D models. Model 3Dthick (magenta curve) prominently synthesizes light r-process nuclei (A < 100), but its production of heavier nuclei beyond the second r-process peak is significantly suppressed. In contrast, Model 3D-kn (red dash-dot curve) generates robust heavyelement abundances, notably featuring a pronounced third peak around A  $\approx$  195 and substantial Actinide yields, while producing comparatively fewer light r-process nuclei. Specifically, the third r-process peak abundance in Model 3D-kn exceeds that of 3Dthick by approximately an order of magnitude. Conversely, 3Dthick overproduces nuclei in the light-element range relative to 3D-kn. The remaining two models, 3D-thin and 3D-kn-p, exhibit intermediate behavior, with abundance patterns situated between these two extremes. Notably, all models reproduce the characteristic r-process peaks near A  $\sim$  80, 130, and 195, though they differ quantitatively in their relative peak amplitudes.

In Table 2 we present the summary of thermodynamic properties of the outflows in various models, as well as some characteristics of the nucleosynthesis patterns produced by these simulations. The outflows from 2D and 3D models exhibit minor differences in their average electron fraction and nucleosynthetic properties, with the most notable discrepancy found in the neutrino-thick models. During the expansion phase, as the temperature drops from 10 GK to 5 GK, the average electron fraction in the fiducial models shows minimal variation. A more pronounced change is observed in the 'kilonova' scenario models; Specifically, the *3D-kn-p* model with a non-axisymmetric perturbation develops an electron fraction about twice that of its unperturbed counterpart.

Finally, in Figure 15 we visualize the ratios of heavy to light elements abundances of the nucleosynthetic yields from our r-process calculations, where the assumed mass number threshold between 'light' and 'heavy' is A=130 (below this peak, the pattern might be highly contaminated by the s-process nucleosynthesis, which is not in the scope of this work). Here we compare these results as a function of the total mass of the outflows, expressed in Solar mass units. It can be seen that the most massive outflows are also mostly abundant in heavy elements, and here our 'kilonova models' are indeed prominent. On the other hand, the fiducial Thin and Thick models produced much

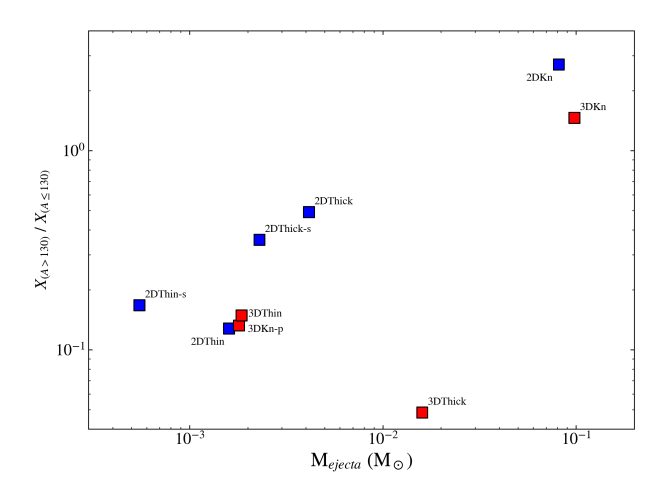


Fig. 15 Mass abundance ratios of heavy to light elements from the nuclear reaction network for all models, as a function of the total mass of the outflows.

less 'heavy' elements, in comparison to 'light' ones, and their total ejecta mass was also small. The Thick models are getting a somewhat larger mass ratio of heavy to light elements, but still, even for the 2D-Thick simulation, the ratio is below 1. We can also notice that the blue points, which represent 2D models are systematically above the red points showing 3D models, which suggests the dimensionality of the GR MHD simulation has a systematic impact on the abundance profiles. The correlation between ejecta mass and heavy element relative abundance is in general visible for both sets of simulations, 2D and 3D.

The only outlier point seen in Fig. 14, is the model 3D-Thick. For this simulation, the heavy element ratio produced in the wind is much smaller than for its 2D representation, at a roughly similar amount of the total outflow mass. The 3D-Thick model resulted in a much larger average electron fraction than for other models ( $< Y_e > \sim 0.432$ , and there is a shift in  $Y_e$  from about 0.3 to 0.4, between the 2D and 3D cases. However, in this simulation, the outflow velocity of the bins with large  $Y_e$  is higher than for those in 2D. In consequence, the nucleosynthesis computed on tracers with high velocities results in their negligible contribution to the heaviest isotopes. The late coming, slow tracers have smaller  $Y_e$ , but they also carry less mass. We attribute this effect to the mechanism of magnetically driven wind, which is responsible for launching the outflows from the surface of the disk (large  $Y_e$ ) and from the inner layers (small  $Y_e$ ). In our Thick models, the magnetic field was initially weaker ( $\beta = 100$ ), which may lead to substantial differences in the process of launching outflows from various layers in the disk.

## 4. Discussion

## 4.1. Heavy element production in the binary merger scenarios

The compact binary mergers are the main sites of r-process heavy element production. However, the detailed outcome of the process heavily depends on the merger progenitor specific type. The binary neutron stars, NS-NS, are found to provide more massive ejecta, where the typical mass of the neutron-rich material is about  $\sim 0.01 - 0.05 M_{\odot}$  (Matsuno et al. 2021). In contrast, the BH-NS mergers ejecta may be less massive, or even negligible, with outflows of  $\sim 0-0.02 M_{\odot}$  as reported by various authors (Drozda et al. 2022; Kobayashi et al. 2023). In our models, the

post-merger systems produce total masses of unbound outflows for the 2D-thin-s, 2D-thin, and 3D-thin models that are systematically smaller than in the other scenarios, and represent the BH-NS post-merger configurations. The electromagnetic counterpart is rarely expected from these events, and it is claimed that only up to  $\sim 1\%$  of these mergers would produce a detectable kilonova (Drozda et al. 2022).

The signal is expected mainly from NS-NS merger events. Their frequency according to the LIGO/Virgo estimates would be around  $\sim 10-1700\,\mathrm{Gpc^{-3}yr^{-1}}$  (Abbott et al. 2023), so roughly 1 event per  $10^4$  yrs per galaxy. The comparison with the BH-NS merger rate gives their number density being 1-2 orders of magnitude lower.

The overall contribution of binary mergers to the chemical enrichment of galaxies and stars is, however, affected by their typical delay times. As reported by Kobayashi et al. (2023), the BH-NS mergers have possibly shorter delay times, because of the more massive progenitor stars that must have evolved quickly to form a BH companion. The NS-NS binary mergers occur within a broad range of delay times that may take a Gyr scale (Skúladóttir & Salvadori 2020). Therefore, it may be hard to enrich the very first stars due to NS-NS merger, and most likely, they are not the only source at the lowest metallicities. Nevertheless, they seem to be the dominant producers of heavy r-process elements in the Milky Way budget (Chen et al. 2024), while the BH-NS mergers would be important only in some niche cases with favorable conditions for launching more massive ejecta.

## 4.2. Chemical enrichment due to mergers

Galactic archaeology is a field of study focused on the structure and evolution of the Milky Way and other galaxies by analysing stellar populations, chemical abundances, and stellar kinematics, which serve as fossil evidence of their history (e.g., Farouqi et al. 2025). While galactic chemical enrichment involves multiple sources like supernovae and winds from massive stars (Lahén et al. 2023), compact binary mergers are considered a primary site for the production of heavy r-process elements ( $A \ge 120$ ; Kobayashi et al. (2023). Traces of this ancient enrichment are found in the atmospheres of extremely metal-poor stars, whose compositions reflect the yields of individual nucleosynthesis events from the early Universe (Hansen et al. 2020).

The ejecta from a BNS or a BH-NS merger are complex, consisting of both early-time dynamical ejecta and later-time winds from a post-merger accretion disk. The simulations presented in this work focus on this disk wind component. Our suite of models shows that these winds can eject between  $M \sim 0.001-0.1 M_{\odot}$  (see Table 2) of r-process material per event. The final nucleosynthetic yields are sensitive to the properties of the central engine and disk; for instance, our models with a lower disk-to-BH mass ratio (e.g., 3D-thin) could be representative of BH-NS merger scenarios and produce a specific abundance pattern. The ejecta are also sufficiently neutron-rich to synthesize a full complement of heavy elements, including a significant lanthanide abundance fraction ( $X_{Lan} \sim 10^{-2}-10^{-4}$ ).

A relevant question is how the yields from our models could account for the galaxy's r-process enrichment. Considering a Milky Way BNS merger rate of  $\sim 20$ -40 Myr<sup>-1</sup> (Colom i Bernadich et al. 2023; Sgalletta et al. 2023), the ejecta masses of  $M \sim 0.001 - 0.1 M_{\odot}$  per event found in our simulations are broadly sufficient to explain a dominant fraction of the Galactic r-process material. A robust assessment, however, requires detailed Galactic Chemical Evolution (GCE) models (e.g., Chen et al. 2025) which can self-consistently incorporate cosmolog-

Table 2 Thermodynamic properties of the outflows and r-process nucleosynthesis characteristics

Model	Total outflow mass $[M_{\odot}]$	$\langle Y_e \rangle_{tr}$ $T = 10 \text{GK}$	$\langle Y_e \rangle_{tr}$ $T = 5 \text{GK}$	$\langle v \rangle$ [c] at $500 r_{\rm g}$	Eu/Fe	$X(57 \le Z \le 72)$ (Lanthanides)
2D-thick-s	$2.3 \times 10^{-3}$	0.388	0.424	0.125	$8.2 \times 10^{-3}$	0.0011
2D-thin-s	$5.5 \times 10^{-4}$	0.382	0.444	0.089	$4.6 \times 10^{-3}$	0.0007
2D-thick	$4.2\times10^{-3}$	0.328	0.389	0.097	$1.7\times10^{-2}$	0.0020
2D-thin	$1.6\times10^{-3}$	0.378	0.448	0.111	$5.5\times10^{-3}$	0.0007
2D-kn	$8.2\times10^{-2}$	0.160	0.189	0.073	1.04	0.0509
3D-thick	$1.6 \times 10^{-2}$	0.420	0.485	0.132	$8.3 \times 10^{-4}$	0.0003
3D-thin	$1.9 \times 10^{-3}$	0.377	0.445	0.100	$1.2\times10^{-2}$	0.0008
3D-kn	$9.8 \times 10^{-2}$	0.191	0.262	0.074	$5.7\times10^{-1}$	0.0265
3D-kn-p	$1.8 \times 10^{-3}$	0.372	0.420	0.193	$4.6\times10^{-2}$	0.0016

**Notes.** Model parameters are given in Table 1. The total mass and the angle-averaged electron fraction are computed for unbound tracers cooled to the NSE breakdown temperature. The velocity (in units of c) is measured at  $500 r_{\rm g}$ . Europium-to-iron number ratios are calculated across all isotopes (not normalized to Solar). The lanthanide abundance fraction is summed over  $57 \le Z \le 72$ .

ical event rates, merger delay-time distributions, and the inhomogeneous mixing of ejecta into the star-forming interstellar medium.

Relative contributions of various progenitor channels- including alternatives such as NS-WD mergers, are also being actively considered (Kaltenborn et al. 2023; Liu et al. 2025; Chen et al. 2024), though their nucleosynthetic yields remain uncertain. Within this context, our work contributes a suite of physically-grounded nucleosynthetic yields for the post-merger disk wind channel. Even within this single channel, we find substantial intrinsic variability in key nucleosynthetic outflow properties; ejecta mass,  $\langle Y_e \rangle$ , and velocity - leading to a broad range of abundance ratios such as Eu/Fe and lanthanide abundance fractions (see Table 2). This intrinsic yield diversity may serve as a natural physical origin for at least part of the chemicalabundance scatter observed among metal-poor halo stars (Cescutti, G. et al. 2015; Wehmeyer et al. 2015). Our results suggest that the observed diversity of r-process enrichment does not necessarily require multiple distinct astrophysical sites, but may instead reflect the intrinsic diversity of merger and disk configurations coupled with the stochastic mixing of their ejecta into the early Galactic medium. These yields serve as a critical and often uncertain input for GCE frameworks, enabling them to test whether the observed diversity of r-process patterns is a natural outcome of the variety of merger events.

#### 4.3. Source 211211A

The unprecedented discovery of a long, 50-second duration, GRB 211211A associated with a kilonova has shown that this event might be associated with a BNS merger. The extended emission of a gamma ray burst exhibited a hard GRB, which was followed by prolonged, softer emission (Rastinejad et al. 2022). The kilonova associated with this event was similar in terms of luminosity, duration, and color to the one observed in the prototypical event GW-GRB 170817, with its progenitor confirmed to be a BNS merger. However, the 211211A source also exhibited several characteristics of the long GRBs, like the hardness ratio being close to their mean value; no associated supernova signal

was detected. Thus, a massive star origin has been ruled out for this source.

From multiwavelength observations, the isotropic equivalent energy of this GRB was  $5 \times 10^{52}$  erg (Gompertz et al. 2023), which seems to be at the higher end of the GRB luminosity distribution (Kumar & Zhang 2015). The afterglow emission was fitted with an additional 3-component kilonova model to elucidate the excess K-band brightness and Optical-NIR data. From the fits, the total r-process ejecta mass was determined to be 0.047  $M_{\odot}$ . The red, purple, and blue ejecta were fitted with velocities of 0.3, 0.1, and 0.3 speed of light, respectively.

Our scenario tested for this source assumed an engine formed after the BNS merger consisting of a rotating black hole with a mass of 8.2  $M_{\odot}$  and spin a = 0.6, surrounded by a remnant accretion disk that is 10 times less massive than a black hole. This engine should produce a powerful, magnetically dominated jet responsible for GRB prompt emission, and also resulted in a substantial mass outflow that might be the source of the 'red' kilonova component. The source of opacity is due to a significant mass fraction of Lanthanides in this scenario, which is 100 times larger compared to our other, fiducial simulations. This scenario is therefore in line with the long binary GRBs discussed recently e.g., by Gottlieb et al. (2025), to originate due to accretion of massive ( $M \ge 0.1 M_{\odot}$ ) disks onto a BH, formed after the transient hypermassive neutron star has collapsed to a BH. The extended duration of the GRB in this case is due to the prolonged accretion in the magnetically arrested state.

This state is, however, not forming in our simulations, while the lanthanide abundance fraction is significantly higher in 2D-kn and 3D-kn than in the other, fiducial models. We speculate that the longer GRB prompt phase might originate due to an eccentric merger, as tested by the 3D-kn-p, see below, Sect. 4.4.

#### 4.4. A long duration post-merger GRB

The duration of a gamma-ray burst (GRB) can be determined by how much time the central engine is active  $t_{\rm GRB} \sim t_{\rm CE}$  (e.g., Beniamini et al. 2020; Zhang 2025). This timescale can reach values of  $t_{\rm CE} \sim 3 \, (\alpha/0.1)^{-1} \, \left( \rho_{\rm d}/5 \times 10^7 \, {\rm g \, cm^{-3}} \right)^{-1/2} \,$  s, depending on the viscous parameter  $\alpha$  and the disk's density  $\rho_{\rm d}$  (e.g., Zhang

2025). In our simulations, the disk's mass can be reduced by magnetically driven outflows. Therefore, we approximate how much the central engine is active by the mean lifetime of the central engine as  $t_{\rm CE} \approx \frac{m_{\rm d}}{\langle M \rangle}$ , where  $\dot{M} = \dot{M}_{\rm in} + \dot{M}_{\rm out}$  is the total mass flux, including both inflow and outflow components. For typical values of  $\dot{M} \sim 10^{-1}\,M_\odot\,{\rm s}^{-1}$ , our massive-disk cases  $(m_{\rm d} \gtrsim 0.1\,M_\odot)$  yield  $t_{\rm CE} \gtrsim 1\,{\rm s}$  (see Fig. 10). For long-duration GRBs arising from binary mergers, we argue that our perturbed model 3D-kn-p, which exhibits low accretion is dominated by outflows  $\langle \dot{M}_{\rm in} \rangle \ll \langle \dot{M}_{\rm out} \rangle \sim 10^{-3}\,M_\odot\,{\rm s}^{-1}$ . Under these conditions, this model could produce a long-lived central engine with  $t_{\rm CE} \gtrsim 800\,{\rm s}$ .

Such perturbations can significantly affect magnetic energy dissipation; as a consequence, the winds are not efficiently driven, and the remaining material accretes without significant ejection. For instance, in collapsar simulations, Mösta et al. (2014) found that a non-axisymmetric perturbed model delayed a magnetically driven explosion, and in addition, a jet is not launched.

# 4.5. The influence of magnetized winds on neutrino emission and the orphan kilonova

Our results indicate that the neutrino luminosity is high in models with a low magnetic flux and/or low initial magnetization. This dominance of neutrino emission persists even in moderately magnetized disks. The weakly magnetized model 3D-Thick, initialized with  $\beta=100$ , shows an early peak in magnetic flux that later decays as  $\Phi_{\rm BH} \propto t^{-1}$ . At t=300 ms, the magnetic flux decreases to  $\Phi_{\rm BH} \sim 10^{27}$  G cm², while the neutrino luminosity reaches  $L_{\nu} \sim 10^{51}$  erg s<sup>-1</sup>. The more magnetized model 3D-Thin, starting from  $\beta=50$ , maintains an almost constant magnetic flux,  $\Phi_{\rm BH} \propto t^{-0.1}$ , and exhibits the neutrino luminosity of  $L_{\nu} \sim 2 \times 10^{50}$  erg s<sup>-1</sup>. This model is more magnetized but about one order of magnitude less massive than the 3D-thick case. The stronger magnetization drives powerful winds, reducing the volume of the neutrino-emitting region and decreasing their thermal energy.

The higher magnetized model 3D-kn, also initialized with  $\beta=50$ , presents a nearly constant magnetic flux of  $\Phi_{\rm BH}\sim 10^{28}~{\rm G~cm^2~(\propto t^{-0.1})}$  and a luminosity of  $L_{\nu}\sim 2.3\times 10^{51}~{\rm erg~s^{-1}}$ . Despite its relatively low spin (a=0.6), this model produces strong mass outflow and intense neutrino emission. In contrast, the perturbed model 3D-kn-p shows that magnetization does not strongly influence the neutrino output. The magnetic flux remains constant but lower ( $\Phi_{\rm BH}\sim 10^{22}~{\rm G~cm^2}$ ), and the neutrino luminosity is about  $L_{\nu}\sim 10^{51}~{\rm erg~s^{-1}}$ . The efficiency of neutrino annihilation can in this case be larger than about 1% (Du et al. 2019), however we speculate that this scenario will rather lead to a weak GRB or an orphan kilonova without a jet.

None of our 3D models reach the magnetically arrested disk (MAD) state, therefore, strong Poynting-dominated jets are not present, despite a high-magnetization funnels,  $\sigma \sim 50$ , produced at evolved state. The neutrino emissivity mainly depends on the internal energy of the disk. As long as winds are not strongly enhanced by magnetization, the neutrino luminosity remains dominant. When mass ejection increases, it proceeds smoothly, so the thermal energy does not vary abruptly. Based on the estimated mass loss, we find that magnetized disks can produce both strong winds and significant neutrino emission.

In several cases, the magnetization decreases with time while the neutrino luminosity becomes dominant. Even in such conditions, when the jet becomes weakly magnetised, it can still successfully penetrate the post-merger environment. Its efficiency does not appear to be strongly affected by the degree of magnetisation in our initial conditions, implying that jet launching can still occur under low-magnetisation scenarios. As shown by e.g., Ruiz & Shapiro (2017) and Hayashi et al. (2025), after a binary merger, the neutrino energy flux can exceed the magnetic energy flux by up to three orders of magnitude. This dominance may challenge jet-launching mechanisms, especially those relying on Poynting-driven jets (e.g., Aguilera-Miret et al. 2024). In contrast, collapsar models show the opposite behaviour: initially, a strong magnetic flux is required to penetrate the stellar envelope (Burrows et al. 2007; Komissarov & Barkov 2009), and the magnetic flux decreases over time while the neutrino luminosity maintains the ram pressure once the jet has cleared the dense material (e.g., Obergaulinger & Aloy 2020).

### 5. Conclusions

In this work, we explored the properties of the GRB central engine suited for post-merger scenarios, with the neutrino-cooled, magnetically driven winds from an accretion disk around a black hole. The system that forms after the binary compact merger event may give a significant contribution to the r-process nucleosynthesis and observable kilonova emission, as well as broadly contribute to the chemical enrichment in the host galaxy.

The main outcomes of our modeling are as follows:

- We obtain plausible scenarios for short GRB engines, with prompt jets powered by neutrino annihilation.
- We confirm that the scenario can model weak jets and magnetically driven wind outflows.
- To model a proper amount of mass loss in the outflows and hence significant wind contributions to the kilonova signal, we need massive disks.
- The kilonova can be modeled with the use of moderate black hole spin; however, this model with the SANE accretion mode results in small power for the Poynting-dominated jets, and hence is not able to reproduce the bright source GRB211211A.
- Our simulation reveals a significant intrinsic diversity in nucleosynthesis yields across different disk configurations, with variations in  $Y_e$ , ejecta mass, and velocities, leading to distinct abundance patterns of light and heavy elements.
- We quantify the Eu/Fe abundance ratio as a key parameter in tracing the chemical enrichment of the Galaxy, and we notice that kilonovae powered by disk winds represent an important channel contributing to this process.

Acknowledgements. We thank Ariadna Murguia-Berthier, Oleg Korobkin and Nicole Lloyd-Ronning for helpful discussions. The project was partially supported by grant 2019/35/B/ST9/04000 from Polish National Science Center. We also acknowledge the PL-Grid infrastructure, Cyfronet AGH, and LUMI supercomputing facility, via grants PLG/2024/017013 and PLL/2024/07/017501, and Warsaw University ICM for their computational resources.

#### References

Abbott, B. P., Abbott, R., Abbott, T. D., et al. 2017a, ApJ, 848, L13
Abbott, B. P., Abbott, R., Abbott, T. D., et al. 2017b, ApJ, 848, L12
Abbott, R., Abbott, T. D., Acernese, F., et al. 2023, Physical Review X, 13, 011048
Aguilera-Miret, R., Palenzuela, C., Carrasco, E., Rosswog, S., & Vigano, D.

Aguilera-Miret, R., Palenzuela, C., Carrasco, F., Rosswog, S., & Viganò, D. 2024, Phys. Rev. D, 110, 083014

Arcones, A. & Thielemann, F.-K. 2023, A&A Rev., 31, 1

Arnould, M., Goriely, S., & Takahashi, K. 2007, Physics Reports, 450, 97 Arunachalam, P., Macias, P., & Foley, R. J. 2025, GRB 230307A Formed No Dust or Was Not a Binary Neutron Star Merger

```
Barnes, J. & Metzger, B. D. 2023, The Astrophysical Journal, 947, 55
Beniamini, P., Duran, R. B., Petropoulou, M., & Giannios, D. 2020, The Astro-
physical Journal Letters, 895, L33
Berger, E. 2011, New A Rev., 55, 1
Berger, E., Fong, W., & Chornock, R. 2013, ApJ, 774, L23
Burrows, A., Dessart, L., Livne, E., Ott, C. D., & Murphy, J. 2007, The Astro-
           physical Journal, 664, 416
 Cescutti, G., Romano, D., Matteucci, F., Chiappini, C., & Hirschi, R. 2015,
A&A, 577, A139
Chen, H.-Y., Landry, P., Read, J. S., & Siegel, D. M. 2025, The Astrophysical
Journal, 985, 154
Chen, M.-H., Li, L.-X., Chen, Q.-H., Hu, R.-C., & Liang, E.-W. 2024, MNRAS,
           529, 1154
Colom i Bernadich, M., Balakrishnan, V., Barr, E., et al. 2023, A&A, 678, A187 Combi, L. & Siegel, D. M. 2023, The Astrophysical Journal, 944, 28 Cowperthwaite, P. S., Berger, E., Villar, V. A., et al. 2017, ApJ, 848, L17 Drozda, P., Belczynski, K., O'Shaughnessy, R., Bulik, T., & Fryer, C. L. 2022,
A&A, 667, A126
Du, S., Peng, F.-K., Long, G.-B., & Li, M. 2019, MNRAS, 482, 2973
Eichler, D., Livio, M., Piran, T., & Schramm, D. N. 1989, Nature, 340, 126
Farouqi, K., Frebel, A., & Thielemann, F.-K. 2025, arXiv e-prints,
            arXiv:2503.18233
arxIV:2503.18253
Fishbone, L. G. & Moncrief, V. 1976, ApJ, 207, 962
Fong, W.-f., Nugent, A. E., Dong, Y., et al. 2022, ApJ, 940, 56
Gammie, C. F., McKinney, J. C., & Tóth, G. 2003, ApJ, 589, 444
Gao, H., Lei, W.-H., & Zhu, Z.-P. 2022, ApJ, 934, L12
Giacobbo, N. & Mapelli, M. 2018, MNRAS, 480, 2011
Gompertz, B. P., Ravasio, M. E., Nicholl, M., et al. 2023, Nature Astronomy, 7,
67
Gottlieb, O., Metzger, B. D., Foucart, F., & Ramirez-Ruiz, E. 2025, ApJ, 984, 77
Hansen, C. J., Koch, A., Mashonkina, L., et al. 2020, A&A, 643, A49
Harten, A. 1983, Journal of Computational Physics, 49, 357
Hayashi, K., Kiuchi, K., Kyutoku, K., Sekiguchi, Y., & Shibata, M. 2025, Phys. Rev. Lett., 134, 211407
Hjorth, J., Sollerman, J., Møller, P., et al. 2003, Nature, 423, 847
Janiuk, A. 2019, ApJ, 882, 163
Kaltenborn, M. A. R., Fryer, C. L., Wollaeger, R. T., et al. 2023, The Astrophysical Lournal, 956, 71
           ical Journal, 956, 71
ical Journal, 956, 71
Kobayashi, C., Mandel, I., Belczynski, K., et al. 2023, ApJ, 943, L12
Komissarov, S. S. & Barkov, M. V. 2009, MNRAS, 397, 1153
Kumar, P. & Zhang, B. 2015, Phys. Rep., 561, 1
Lahén, N., Naab, T., Kauffmann, G., et al. 2023, MNRAS, 522, 3092
Lattimer, J. M. & Schramm, D. N. 1974, ApJ, 192, L145
Levan, A. J., Gompertz, B. P., Salafia, O. S., et al. 2024, Nature, 626, 737
Li, L.-X. & Paczyński, B. 1998, ApJ, 507, L59
Lippuner, J. & Roberts, L. F. 2017, The Astrophysical Journal Supplement Series 232, 18
ries, 233, 18
Liu, X.-X., Lü, H.-J., Chen, Q.-H., Du, Z.-W., & Liang, E.-W. 2025, The Astro-
Liu, A.-A., Lu, H.-J., Chen, Q.-H., Du, Z.-w., & Liang, E.-w. 2023, The Astrophysical Journal Letters, 988, L46

Matsuno, T., Hirai, Y., Tarumi, Y., et al. 2021, A&A, 650, A110

Mösta, P., Richers, S., Ott, C. D., et al. 2014, ApJ, 785, L29

Murguia-Berthier, A., Noble, S. C., Roberts, L. F., et al. 2021, ApJ, 919, 95

Nagakura, H., Zaizen, M., Liu, J., & Johns, L. 2025, Phys. Rev. D, 111, 043028

Narayan, R., Paczynski, B., & Piran, T. 1992, ApJ, 395, L83

Nishimura, N., Takiwaki, T., & Thielemann, F.-K. 2015, The Astrophysical Journal of the 1000
nal, 810, 109
Noble, S. C., Gammie, C. F., McKinney, J. C., & Del Zanna, L. 2006, ApJ, 641,
626
Nouri, F. H., Janiuk, A., & Przerwa, M. 2023, ApJ, 944, 220
Obergaulinger, M. & Aloy, M. A. 2020, MNRAS, 492, 4613
Ott, C. D., Abdikamalov, E., O'Connor, E., et al. 2012, Phys. Rev. D, 86, 024026
Palenzuela, C., Liebling, S. L., Neilsen, D., et al. 2015, Phys. Rev. D, 92, 044045
Piran, T. 2004, Reviews of Modern Physics, 76, 1143
Pontzen, A., Deason, A., Governato, F., et al. 2010, MNRAS, 402, 1523
Rastinejad, J. C., Gompertz, B. P., Levan, A. J., et al. 2022, Nature, 612, 223
Reichert, M., Obergaulinger, M., Aloy, M. A., et al. 2022, Monthly Notices of the Royal Astronomical Society 518, 1557
the Royal Astronomical Society, 518, 1557
Ristić, M., Barker, B. L., Cupp, S., et al. 2025, arXiv e-prints, arXiv:2509.03003
Rosswog, S. & Liebendörfer, M. 2003, MNRAS, 342, 673
Ruiz, M. & Shapiro, S. L. 2017, Phys. Rev. D, 96, 084063
Sgalletta, C., Iorio, G., Mapelli, M., et al. 2023, Monthly Notices of the Royal
Sgalletta, C., Iorio, G., Mapelli, M., et al. 2023, Monthly Notices of the Royal Astronomical Society, 526, 2210
Siegel, D. M., Barnes, J., & Metzger, B. D. 2019, Nature, 569, 241
Siegel, D. M. & Metzger, B. D. 2017, Phys. Rev. Lett., 119, 231102
Siegel, D. M., Mösta, P., Desai, D., & Wu, S. 2018, ApJ, 859, 71
Skúladóttir, A. & Salvadori, S. 2020, A&A, 634, L2
Tanvir, N. R., Levan, A. J., Fruchter, A. S., et al. 2013, Nature, 500, 547
Timmes, F. X. & Swesty, F. D. 2000, ApJS, 126, 501
Vigna-Gómez, A., Neijssel, C. J., Stevenson, S., et al. 2018, MNRAS, 481, 4009
Wang, X., Clark, A. M., Ellis, J., et al. 2021, The Astrophysical Journal, 923, 210
           219
  Wang, X. I., Yu, Y.-W., Ren, J., et al. 2024, The Astrophysical Journal Letters,
           964, L9
  Wehmeyer, B., Pignatari, M., & Thielemann, F.-K. 2015, Monthly Notices of the
Royal Astronomical Society, 452, 1970
Woosley, S. E. 1993, ApJ, 405, 273
Woosley, S. E. & Heger, A. 2006, ApJ, 637, 914
Yang, J., Ai, S., Zhang, B.-B., et al. 2022, Nature, 612, 232
Zhang, B. 2025, Journal of High Energy Astrophysics, 45, 325
Zhong, S.-Q., Li, L., & Dai, Z.-G. 2023, The Astrophysical Journal Letters, 947, 121
 Zhu, J.-P., Wang, X. I., Sun, H., et al. 2022, The Astrophysical Journal Letters,
```

936, L10

## Appendix A: Recovery method

We use the EOS adapted from Helmholtz tables, with  $P(\rho, T, Y_e)$ and  $\epsilon(\rho, T, Y_e)$ , where  $Y_e$  is the electron fraction. It is usable for a wide range of densities and temperatures. The evolving electron fraction is giving an additional source term to the energy equation.

The GR MHD code solves system of equations in the form

$$\partial_t \mathbf{U}(\mathbf{P}) = -\partial_i \mathbf{F}^i(\mathbf{P}) + \mathbf{S}(\mathbf{P}) \tag{A.1}$$

where  $\mathbf{U}(\mathbf{P})$  are conserved variables that evolve through the fluxes at cell boundaries and source terms. Here P are the 'primitive variables, which are subject to the EOS.

Explicit form of primitive and conserved variables, fluxes, and source terms, is:

$$\begin{split} \mathbf{P} &= [\rho, \ \mathcal{B}^k, \ \tilde{u}^i, \ Y_e, \ T] \\ \mathbf{U}(\mathbf{P}) &= \sqrt{-g} [\rho u^t, \ T_t^t + \rho u^t, \ T_j^t, \ B^k, \ \rho Y_e u^t] \\ \mathbf{F}^i(\mathbf{P}) &= \sqrt{-g} [\rho u^i, \ T_t^i + \rho u^i, \ T_j^i, \ (b^i u^k - b^k u^i), \ \rho Y_e u^i] \\ \mathbf{S}(\mathbf{P}) &= \sqrt{-g} [0, \ T_{\lambda}^{\kappa} \Gamma_{t\kappa}^{\lambda} + Q u_t, \ T_{\lambda}^{\kappa} \Gamma_{t\kappa}^{\lambda} + Q u_i, \ 0, \ \mathcal{R}] \end{split}$$

Here  $B^i = \mathcal{B}^i/\alpha = F^{it}$  is magnetic field three-vector, and  $\tilde{u}^{\mu} =$  $(\delta_{\nu}^{\mu} + n^{\mu}n_{\nu})u^{\nu}$  is the projected four-velocity, where the orthogonal frame velocity is  $n_{\mu} = [-\alpha, 0, 0, 0], n^{\mu} = [1/\alpha, -\beta^{i}/\alpha]$ , with lapse  $\alpha = 1/\sqrt{g^{tt}}$ , and shift function  $\beta^i = -g^{ti}/g^{tt}$ .

In non-relativistic MHD, both  $P \rightarrow U$  and  $U \rightarrow P$  have a closed-form solution. In GRMHD U(P) is a complicated, nonlinear relation. Inversion **P**(**U**) is calculated once or twice in every time step, numerically, by the recovery scheme.

There exist a number of inversion schemes, based on specific transformations between these five independent variables (Siegel et al. 2018). Inversion is a complex procedure specifically for a non-adiabatic relation of the pressure with density (ie. if the EOS is not given by the so called gamma-law,  $p(\rho) = (\gamma - 1)\rho\epsilon$ ). The numerically computes tabulated EOS can be of general form of

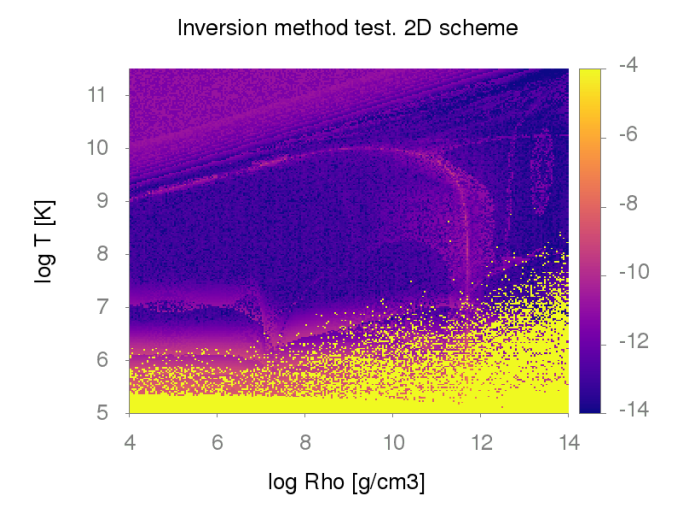
- 1-parameter  $\epsilon(\rho)$ ,  $P_{\epsilon}(\rho)$
- 2-parameter  $\epsilon(\rho, T), P_{\epsilon}(\rho, T)$  3-parameter  $\epsilon(\rho, T, Y_e), P_{\epsilon}(\rho, T, Y_e)$

In the former work Janiuk (2019), we used the code based on the 2-parameter tabulated EOS. In the current work, we use the 3-parameter one.

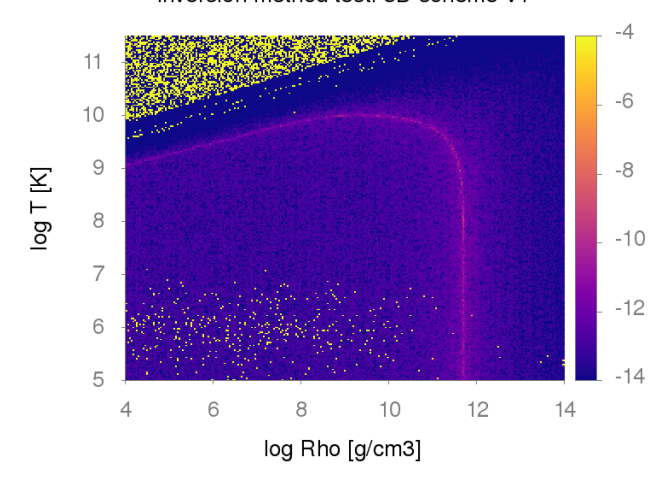
We need to recover the primitive variables, as they are required to construct  $T^{\mu\nu}$  and flux terms in fluid evolution. Recovery methods can lead to bounded or unbounded solution, and the typically used Newton-Raphson methods are unbounded. They exhibit a faster convergence but are less stable, therefore in this work, for some parameter range, we switch to the bracketed rootfinding method of Palenzuela et al. (2015) which is slower but more robust. We combined these two methods in our code, to effectively obtain minimum errors for a wide range of temperatures and densities.

In Figure A.1 we present a comparison of our convergence tests made for the 3D scheme and the Palenzuela scheme. The 3D scheme (method-v1) computes specific internal energy from state vector x and conservatives as in Eq. (25) in Cerda-Duran et al. (2008). We solve  $f_3$ , as the system is reduced to solve 3 equations, on  $\Gamma$ , z, and T, by adding a constraint on the internal energy given by EOS tables, namely:

$$f_1: [\tau + D - z - B^2 + \frac{B^i Q_i}{2z^2} + \rho]\Gamma^2 - \frac{B^2}{2} = 0$$







## Inversion method test. Palenzuela

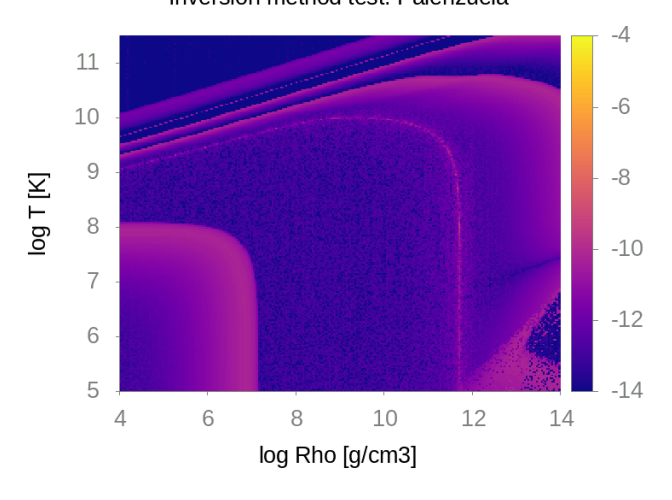


Fig. A.1 Convergence tests results for the 2D, 3D recovery scheme, and Palenzuela scheme.

$$f_2: [(z+B^2)^2 - Q^2 - \frac{2z+B^2}{z^2} (B^i Q_i)^2] \Gamma^2 - (z+B^2)^2 = 0$$
  
$$f_3: \epsilon - \epsilon(\rho, T, Y_e) = 0$$

Here the temperature is employed directly as an unknown through  $\epsilon(\Gamma, z, T) = h - 1 - \frac{P}{\rho} = \frac{z - D\Gamma - \rho\Gamma^2}{D\Gamma}$  and does not require inversion of the EOS. Notice here notation:  $Q_{\mu} = -n_{\mu}T_{\mu}^{\nu} = \alpha T_{\mu}^{t}$  is energy-momentum density,  $\Gamma$  is Lorentz factor, z is enthalpy,  $D = -\rho n_{\mu} u^{\mu} = \alpha \rho u^{t}$  is comoving density, and  $\tau = -(n_{\mu} n_{\nu} T^{\mu\nu} + D)$ .

In 'Palenzuela' scheme, the code is solving 1D equation, for the rescaled variable

$$\chi = \frac{\rho h \gamma^2}{\rho \gamma}$$

Other quantities are also rescaled, accordingly, to give Lorentz factor, and we give the brackets for  $\chi$ :

$$2 - 2 \frac{Q_{\mu} n^{\mu} + D}{D} - \frac{\mathcal{B}^2}{D} < \chi < 1 - \frac{Q_{\mu} n^{\mu} + D}{D} - \frac{\mathcal{B}^2}{D}$$

The equation

$$f(\chi) = \chi - \tilde{\gamma}(1 + \tilde{\epsilon} + \frac{\tilde{P}}{\tilde{\rho}}) = 0$$

is solved, with  $\tilde{P} = P(\tilde{\rho}, \tilde{\epsilon}, Y_e)$  found in tables.

The tests presented in Figure A.1 were performed over a broad range of temperatures and densities. We show the value of relative error, summed over primitive variables, recovered through the alternative schemes. The parameters used were: electron fraction  $Y_e = 0.1$ , Lorentz factor  $\Gamma = 2$ , gas-to-magnetic pressure ratio  $p_{gas}/p_{mag} = 10^5$ . Conserved variables were derived in Kerr metric, then the primitives were perturbed by a factor of 1.05. The variables recovered through the recovery scheme are compared to the unperturbed, to calculate error of  $Err = \Sigma_{k=0,NPR}(P_k - \bar{P}_k)^2$ .

For the 3D scheme, we checked two versions, and the test shown in the plot presents better convergence. As an alternative, instead of the specific internal energy, we can compute pressure from state vector x and conservatives and then solve for  $f_3$ , as done e.g. in Murguia-Berthier et al. (2021). This version however good for high temperatures, showed bad convergence for temperatures below  $T \leq 10^7$  K. Similarly, the 2D method presented in Murguia-Berthier et al. (2021) showed bad convergence at low temperatures however in our case the method is satisfactory for most of temperature range at low densities. The bracketed 'Palenzuela' scheme is behaving well, and was used at high temperature and low density regime.

#### **Appendix B: Neutrino treatment**

The neutrino leakage scheme computes a gray optical depth estimate along radial rays for electron neutrinos, antineutrinos, and heavy-lepton neutrinos (nux),

$$\tau(r,\theta,\phi) = \int_{r}^{R} \sqrt{\gamma_{rr}} \bar{\kappa}_{\nu_{i}}$$
 (B.1)

and then computes local energy and lepton number loss terms, Q and  $\mathcal{R}$ , that are evolved via source terms by the GR MHD scheme Eq. A.1.

The scheme is based on equations provided by Rosswog & Liebendörfer (2003), giving the neutrino number emission rates and energy emission rates per unit volume. These effective rates account for locally produced neutrinos as well as the diffusive terms. The source code of the leakage scheme has been downloaded from <a href="https://stellarcollapse.org">https://stellarcollapse.org</a> and we implemented it in our GR MHD code, HARM\_EOS, where it is coupled to the inversion procedures. The scheme captures effects of deleptonization, neutrino cooling and heating and enables approximate predictions for the neutrino luminosities. Details and implementation to the core-collapse supernovae simulations can be found in Ott et al. (2012).